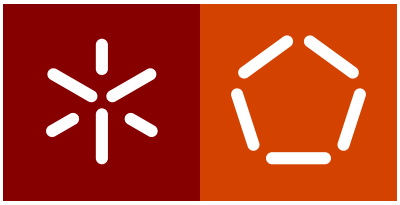

Universidade do Minho
Escola de Engenharia
Departamento de Informática

Tiago Moreira Machado

Development and analysis of mathematical models to study metabolic constraints and capacities in different photosynthetic types

October 2022

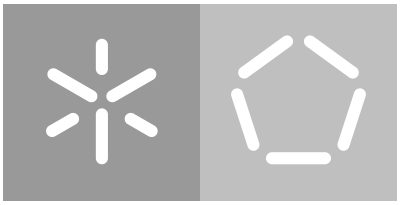

Universidade do Minho
Escola de Engenharia
Departamento de Informática

Tiago Moreira Machado

Development and analysis of mathematical models to study metabolic constraints and capacities in different photosynthetic types

Master dissertation
Master Degree in Bioinformatics

Dissertation supervised by
Óscar Manuel Lima Dias
Nadine Töpfer

October 2022

DIREITOS DE AUTOR E CONDIÇÕES DE UTILIZAÇÃO DO TRABALHO POR TERCEIROS

ACKNOWLEDGEMENTS

As I reach the end of another major step in my life, I would like to thank to all those who supported me during my journey.

To my advisors, without which this work would not have been possible. To Dr. Nadine Töpfer, for her unyielding support, her kindness and her small and big lessons. Thank you for trusting me and making me grow. And to Dr. Óscar Dias for his advice, guidance and availability. Without your teaching, I wouldn't be working on this topic I cherish today.

To the Leibniz Institute of Plant Genetics and Crop Plant Research (IPK) for financing this work through my employment as a research assistant under the Metabolic Systems Interactions research group. To the European Union who funded this work by granting me an Erasmus+ Internship scholarship.

To all the members of the MSI group for integrating me so effortlessly, for helping me when I needed it and for all the lively discussions. Working with you was and is a pleasure.

To all the friends and helpful colleagues I found at the IPK Gatersleben for making everyday life joyful and keeping all semblance of solitude at bay. Thank you for being an unexpected gift, and for the crazy adventures.

To all my buddies at the University of Minho, in particular Miguel Barros, Mónica Fernandes and Tiago Silva. Thank you for keeping me sane when nothing else would or could.

To my friends Adriana Guerreiro and Filipa Arega for being a shoulder for my tears, an ear for my gossip and a home to party on, not necessarily in this order. I don't know how you have put up with me all this time, but it makes me very happy. To my friend Daniela Ferreira for making me question myself and think beautiful thoughts. Thank you for helping me be myself.

To my family, without which I would not be possible. To my grandparents for being home. To my mother for her unconditional support. To my father, for always being there when I need him. To my sisters, Rita and Maria, for healing me with their love.

A heartfelt thank you to all those not mentioned here, but in one way or another made themselves present and supported me during this journey. THANK YOU!

STATEMENT OF INTEGRITY

I hereby declare having conducted this academic work with integrity. I confirm that I have not used plagiarism or any form of undue use of information or falsification of results along the process leading to its elaboration.

I further declare that I have fully acknowledged the Code of Ethical Conduct of the University of Minho.

ABSTRACT

Climate change and a growing human population necessitate improved crop adaptability and yield. Improving photosynthesis is one promising route to boosting plant productivity. Photosynthesis is hampered by the dual activity of its main CO_2-fixing enzyme ribulose-1,5-bisphosphate carboxylase/oxygenase (Rubisco). The enzyme side-reacts with O_2, leading to the production of a toxic byproduct, which must be expensively recycled through the photorespiratory pathway. Rubisco's oxygenation rate depends on the $CO_2 : O_2$ ratio and increases under high temperatures. In C_3 plants, which make up 90% of the known plant species, this phenomenon can decrease photosynthetic efficiency by an estimated fourth. C_4 plants have evolved a carbon-concentration mechanism that suppresses photorespiration by spatially separating initial carbon fixation and re-fixation by Rubisco. Initial carbon fixation occurs in the mesophyll cells, while decarboxylation and carbon fixation by Rubisco occurs in the bundle sheath cell and releases pyruvate or phosphoenolpyruvate which then moves back to the mesophyll cells for the next cycle. To successfully engineer C_4 metabolism in C_3 plants, it is important to obtain a quantitative understanding of both the energetics and distribution of metabolic fluxes of this metabolic cycle. Here, we tackle this question by analysing a large-scale metabolic model, consisting of mesophyll and bundle sheath cells connected through the exchange of cytosolic metabolites. We parameterized the model for the main C_4 crop maize (*Zea mays*) by using biochemical and anatomical constraints derived from the literature. These constraints also enable the model to correctly predict the appearance of the C_4 cycle, different C_4 subtypes and decarboxylation enzyme co-activity. Accounting for the volumetric ratio between the two cell types leads to more accurate predictions of C_2 photosynthesis, a triose phosphate-3-phosphoglycerate shuttle between the cell types, mesophyll-specific nitrate reduction, choice of decarboxylation enzyme, the ratio of ATP production between the cell types, cell type-specific cyclic or linear electron transport activity and biomass production. Thus, our modelling approach can guide biological engineering strategies to implement C_4 photosynthesis into other plant systems to ultimately improve crop productivity.

Keywords: Anatomical Constraints; C_4 Photosynthesis; Constraint-Based Modelling; *Zea mays*.

RESUMO

As alterações climáticas e o crescimento da população humana tornam necessário uma melhor adaptabilidade e rendimento agrícola. Melhorar a fotossíntese é uma via promissora para aumentar a produtividade vegetal. A fotossíntese é dificultada pela dupla actividade da principal enzima fixadora de CO_2, a ribulose-1,5-bisfosfato carboxilase/oxigenase (Rubisco). A enzima reage paralelamente com O_2, levando à produção de um subproduto tóxico, que é reciclado através da via fotorrespiratória. A taxa de oxigenação da Rubisco depende do rácio CO_2 : O_2 e aumenta com temperaturas elevadas. Nas plantas C_3, que constituem 90% das espécies vegetais conhecidas, este fenómeno pode diminuir a eficiência fotossintética em um quarto. As plantas C_4 desenvolveram um mecanismo de concentração de carbono que suprime a fotorrespiração separando espacialmente a fixação inicial de carbono e a refixação pela Rubisco. A fixação inicial de carbono ocorre nas células do mesofilo, enquanto a descarboxilação e a fixação de carbono pela Rubisco ocorre nas células da bainha do feixe e liberta piruvato ou fosfoenolpiruvato, que depois se desloca de volta para o mesofilo para o ciclo seguinte. Para incorporar o metabolismo C_4 em plantas C_3, é importante obter uma compreensão quantitativa da produção de energia e da distribuição dos fluxos metabólicos deste ciclo. Neste trabalho abordamos esta questão através da análise de um modelo metabólico em grande escala, constituído por uma célula do mesofilo e da bainha de feixe conectadas pela troca de metabolitos citosólicos. Parametrizámos o modelo com restrições bioquímicas e anatómicas de milho (*Zea mays*) derivadas da literatura. Estas restrições permitem ao modelo prever o ciclo e diferentes subtipos de fotossíntese C_4 e co-actividade de enzimas de descarboxilação. A inclusão do volume celular leva a previsões mais precisas de componentes metabólicos tais como a fotossíntese C_2, o transportador triose fosfato-3-fosfoglicerato, a redução de nitrato no mesofilo, a escolha da enzima de descarboxilação, o rácio entre a produção de ATP nas células, a actividade cíclica ou linear de transporte de electrões e a produção de biomassa. Assim, a nossa abordagem de modelação pode guiar estratégias de engenharia biológica para implementar a fotossíntese C_4 noutros sistemas vegetais e melhorar a produtividade agrícola.

Palavras-Chave: Restrições Anatómicas; Fotossíntese C_4; Modelação Baseada em Restrições; *Zea mays*.

CONTENTS

ACRONYMS

2-PG	2-phosphoglycerate
3-PGA	3-phosphoglycerate
ADP	Adenosine Diphosphate
AspAT	aspartate aminotransferase
ATP	Adenosine Triphosphate
ATPase	ATP Synthase
BS	Bundle Sheath
C	carbon
CAM	Crassulacean Acid Metabolism
CBB	Calvin-Benson-Basham
CBM	Constraint-based Modelling
CO_2	carbon dioxide
COBRA	COnstraints-Based Reconstruction and Analysis
COBRApy	COnstraints-Based Reconstruction and Analysis for Python
cyt b6f	Cytochrome b6f Complex
DPG	3-phospho-D-glyceroyl phosphate
$FADH_2$	flavin adenine dinucleotide
FBA	Flux-Balance Analysis
Fd	ferredoxin
FNR	Ferrodoxin-NADP+ Reductase
FQR	Fd-PQ oxidoreductase
FVA	Flux Variability Analysis

G3P	3-phospho-D-glycerate
GAP	D-glyceraldehyde 3-phosphate
GDC	Glycine Decarboxylase
GDH	Glutamate Dehydrogenase
GES	Genome Scale
GOGAT	Glutamate Synthase
GS	Glutamine Synthase
H_2O	water
KEGG	Kyoto Encyclopedia of Genes and Genomes
M	Mesophyll
N	nitrogen
NAD^+	nicotinamide adenine dinucleotide oxidized
NAD-ME	NAD-dependent Malic Enzyme
NADH	nicotinamide adenine dinucleotide reduced
$NADP^+$	nicotinamide adenine dinucleotide phosphate oxidized
NADP-ME	NADP-dependent Malic Enzyme
NADPH	nicotinamide adenine dinucleotide phosphate reduced
Nda2	type 2 NADPH:PQ oxidoreductase
NDH	type 1 NADPH dehydrogenase
NH_4^+	ammonium
NiR	Nitrite Reductase
NO_2^-	nitrite
NO_3^-	nitrate
NR	Nitrate Reductase
O_2	oxygen
OAA	oxaloacetate

PC	plastocyanin
PEP	Phosphoenolpyruvate
PEPC	Phosphoenolpyruvate Carboxylase
PEP-CK	Phosphoenolpyruvate Carboxykinase
pFBA	parsimonious enzyme usage FBA
PPDK	Pyruvate, phosphate dikinase
PQ	plastoquinone
PQH2	plastohydroquinone
PSI	Photosystem I
PSII	Photosystem II
Rubisco	Ribulose-1,5-bisphosphate carboxylase-oxygenase
RuBP	Ribulose-1,5-bisphosphate
TCA	Tricarboxylic Acid
WUE	Water-Use Efficiency

LIST OF FIGURES

LIST OF TABLES

1

INTRODUCTION

1.1 MOTIVATION AND CONTEXT

Climate change is predicted to have direct impacts on agricultural production over the course of the 21st century [1]. The main effects of climate change that impact agriculture are well documented: increases in atmospheric carbon dioxide (CO_2) concentration; changes to temperature, precipitation and solar exposure levels; rising sea levels; and more severe and frequent extreme climatic events. The combination of these factors contributes to negative impacts on agricultural production worldwide, making agriculture one of the most endangered activities by climate change [2, 3].

Due to climate change, the decline of agricultural production will negatively affect global food production [4]. This problem is further magnified by an estimated growth of the world human population to approximately 9.7 billion by 2050 [5], which will lead to an estimated increase in food demand between 59 and 98% [6].

Reducing the impact of climate change on agriculture and increasing agricultural productivity is vital to safeguarding food security over the next century and reducing hunger and malnutrition, particularly in developing countries [7]. This calls for the need to implement crop breeding approaches that will help develop climate-resilient crops with better adaptability and productivity under stress conditions [3].

One fundamental component of plant metabolism that can increase yield is photosynthesis. Photosynthesis is the process during which light is converted into the carbohydrates' chemical energy using CO_2 and water (H_2O) [8]. It is the leading supplier of carbon and energy required to synthesise the organic compounds that drive plant growth and development [9]. Additionally,

photosynthesis core metabolic pathways are highly conserved across a wide range of plant species and they are one of the best-studied processes. The three known types of photosynthesis are the C_3, C_4 and Crassulacean Acid Metabolism (CAM) photosynthesis. These photosynthetic types differ in their carbon fixation strategies, with C_3 being the most frequent type, while C_4 evolved in plants under hot, low CO_2 environments and CAM in arid biomes, in which plants suffered from water limitation [10]. Additionally, these pathways display different resource requirements, with nitrogen (N) being relevant due to its role in protein synthesis [11]. Thus, boosting plant photosynthetic efficiency is a target for improving crop productivity. However, past efforts to improve photosynthetic efficiency have not been sufficient to improve productivity to the estimated required levels and future outcomes depend on a further understanding of the photosynthetic process [12, 13].

Research on photosynthesis finds a powerful tool in systems biology and computational modelling. These disciplines provide techniques for the in silico representation of metabolic pathways and cellular organization, through the construction of metabolic models and optimisation routines [14]. One of these techniques is Constraint-based Modelling (CBM). A key feature of CBM is the dependence only on reaction stoichiometry and not kinetic parameters for model building and simulation, allowing metabolism to be simulated at a large- and even genome-scale [15]. The effects of different environments on metabolism can be investigated through this framework. More concretely, such a large-scale model can be employed to study the metabolism of photoautotrophic plant cells, allowing the study of the effect of environmental changes on photosynthetic metabolism and comparing different photosynthetic pathways regarding the metabolic response to these changes [16]. Overall, the use of CBM applied to the study of photosynthesis will allow us to better understand metabolic responses to changes in the environment and provide insights into how to engineer these pathways toward a greater photosynthetic efficiency [17].

1.2 Goals

The main goal of this thesis is to compare different types of photosynthesis regarding their constraints and capacities, particularly the effect of anatomical constraints upon carbon, nitrogen and energetic metabolism, using CBM.

In detail, the objectives are:

- Review the relevant literature as to existing plant leaf models;
- Set up photoautotrophic growing leaf models capable of different types of photosynthesis;
- Implement novel anatomical constraints into the developed photosynthetic model;
- Compare anatomy-constrained model predictions against the bibliography;
- Evaluate energy metabolism, biomass production and cell-specific distributions of carbon and nitrogen metabolism in C_4 photosynthesis;

1.3 Thesis organization

In **Chapter 2** the literature review will be presented with a detailed state of the art regarding the present work. The biological problem will be presented first, exploring our current knowledge of photosynthesis and its known types and subtypes, alongside their benefits and limitations. Second, we will review plant energy metabolism, specifying the known types of metabolic energy and where they can be contained and spent. Third, we will then overview nitrogen metabolism, with a specific focus on C_4 nitrate assimilation. Fourth, we will overview CBM approaches, detailing both the architecture of stoichiometric models and simulation frameworks. Fifth, we will review existing stoichiometric models of plant metabolism and further specify existing models for modelling photoautotrophic plant leaf cells. Lastly, we will revise the literature for the impact of leaf anatomical constraints on C_4 metabolism, and their potential applications.

In **Chapter 3** we will explain how the metabolic models used in the present work were built and curated. Additionally, we will also detail how the anatomical constraints were implemented into the models. In the end, we will review the techniques used to generate and analyse flux solutions from the models

In **Chapter 4** the results of this work will be presented. We will overview all obtained data regarding maize biomass composition, C_4 cycle, nitrogen metabolism and assimilation, choice of decarboxylation enzymes, type of electron transport and ATP and biomass production. Throughout the chapter, a discussion of the results will be presented against bibliographic sources.

In **Chapter 5** we will showcase the final conclusions of the project and finalize with discussing future research directions.

2

STATE OF THE ART

2.1 PHOTOSYNTHESIS

Oxygenic photosynthesis is one of the most important metabolic processes in the world, with almost all life depending on it either directly or indirectly. Through photosynthetic organisms such as plants, algae and cyanobacteria can utilize light energy to generate organic molecules, such as glucose, from CO_2 and H_2O, while releasing molecular oxygen (O_2) into the atmosphere. In equation (1) we present the generic equation for photosynthesis [18].

$$6\ \mathrm{CO_2} + 12\ \mathrm{H_2}O + \text{light energy} \rightarrow \mathrm{C_2}H_{12}O_6\ + 6\ \mathrm{O_2} + 6\ \mathrm{H_2}O \tag{1}$$

The reactions of oxygenic photosynthesis take place, in the cells of algae and plant leaves, inside organelles termed chloroplasts. Chloroplasts are surrounded by a double membrane, inside of which there is a membrane system referred to as thylakoids. These structures separate an internal space, called lumen, from an outer space, called stroma, which holds the necessary enzymes for carbon (C) fixation. Embedded in the thylakoid membranes are large protein complexes of which Photosystem I (PSI), Photosystem II (PSII), Cytochrome b6f Complex (cyt b6f) and ATP Synthase (ATPase) are the main enzymatic complexes for light energy absorption and transformation [10].

Chlorophyll (green pigments) and carotenoids (yellow-to-orange pigments) are parts of both PSI and PSII complexes and these pigments are responsible for absorbing light energy, which is then delivered to the PSI and PSII reaction centres through pigment-protein antennas. This energy is then converted into redox chemical energy, with a small part being dissipated as heat and chlorophyll fluorescence. Through this process, H_2O is oxidised to O_2, with the production of Adenosine Triphosphate (ATP) and nicotinamide adenine dinucleotide phosphate

reduced (NADPH). These reactions all occur in the thylakoid membrane and are collectively designated as the “light reactions” of photosynthesis [19].

The products of the light reactions (ATP and NADPH) are then used for CO_2 assimilation in the stroma in the “dark reactions” of photosynthesis. It is worth noting that the dark reactions are active in the presence of light; the designation originates because they are not directly driven by light absorption [20]. The CO_2 is obtained from the atmosphere by diffusion through the stomata, small pores which regulate gas exchange in the plant’s leaves. The assimilation of CO_2 occurs via the Calvin-Benson-Basham (CBB), resulting in the reduction of CO_2 into carbohydrates, such as sucrose and starch (Fig. 1) [21].

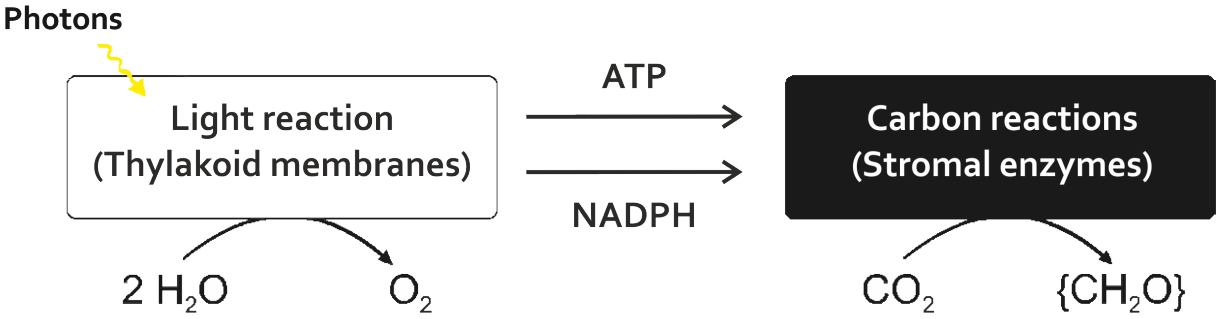

Figure 1 – Simplified scheme for the relation between the “Light Reaction” and the “C reactions” or “Dark reactions”. The ATP and NADPH provided by the light reactions using light and H_2O, power the formation of CH_2O which stands for a simplified carbohydrate unit, while releasing O_2. Adapted from [10]

Plants have evolved three main pathways for the assimilation of CO_2, reflecting adaptation to various environmental conditions: C_3, C_4 and CAM. We will elaborate upon these photosynthetic types in the following chapters.

2.1.1 C_3 PHOTOSYNTHESIS

C_3 photosynthesis is the most widespread form of C assimilation in photosynthetic organisms, accounting for the assimilation of about 15% of the C in the atmosphere every year [22]. In C_3 species CO_2 assimilation occurs practically in all leaf mesophyll cells, which are in direct contact with the intercellular air space that is connected to the atmosphere via stomatal openings in the epidermis [23]. In the first step, the enzyme Ribulose-1,5-bisphosphate carboxylase-oxygenase (Rubisco) catalyses the carboxylation of CO_2 acceptor molecule Ribulose-1,5-bisphosphate (RuBP), forming 3-phosphoglycerate (3-PGA) which consists of three C atoms, giving rise to

the name "C_3 cycle" [8]. Due to the contact with the outer environment, Rubisco also catalyses the oxygenation of RuBP in which it reacts with oxygen, forming 2-phosphoglycerate (2-PG) (Fig. 3 (I)). However, accumulation of 2-PG can lead to a reduction in RuBP regeneration and is therefore toxic to plants. Formation of 2-PG due to the oxygenation activity of Rubisco activates recycling of 2-PG by the photorespiratory C oxidative pathway, which prevents the accumulation of 2-PG and recovers 75% of fixed C lost due to oxygenation while the remaining 25% are released as CO_2. Photorespiration is also referred to as the "C_2 cycle" due to being essentially a recovery pathway triggered by 2-PG, a two-C molecule [24]. Besides the loss of efficiency of C fixation, the C_2 cycle also incurs additional ATP and NADPH costs associated with the re-fixation of C and re-assimilation of N [25]. The ratio of carboxylation to oxygenation of Rubisco is dependent on the CO_2 : O_2 ratio in the cell. Additionally, the oxygenase activity of Rubisco is temperature-dependent, increasing with temperature. Rubisco sensitivity to O_2 makes it so that the efficiency of the C_3 pathway decreases as atmospheric CO_2 decreases and temperature increases, creating an evolutionary pressure on the photosynthetic pathway for increased efficiency under low atmospheric CO_2 and/or high temperatures [26].

2.1.2 C_2 PHOTOSYNTHESIS

A phenotype between C_3 and C_4 plants exists corresponding to an intermediate evolutionary stage corresponding to a dual-celled photorespiratory glycine shuttle [27]. During evolution, after the Bundle Sheath (BS) cells become photosynthetically engaged, they acquire increased numbers of chloroplasts and mitochondria. BS mitochondria migrate to the centripetal region of the cell, followed by chloroplast, giving rise to "proto-Kranz" anatomy [28]. This leads to the reduction of Glycine Decarboxylase (GDC) activity in the Mesophyll (M) cell, while BS GDC activity is increased. The enzyme GDC is a key component in the photorespiratory pathway, from whose activity also results in the release of CO_2 and ammonium (NH_4^+). Its migration to the BS translates into glycine, originating from the M cell photorespiratory salvage pathway, being transported from M to BS to serve as a substrate for GDC, and the resulting CO_2 enters the CBB cycle in the BS chloroplast, resulting in an initial carbon concentrating mechanism around Rubisco [29]. This metabolic conformation is termed C_2 photosynthesis, due to glycine

being a 2 C molecule, and represents an important intermediate step before a full-fledged C_4 cycle is developed [30].

2.1.3 C_4 PHOTOSYNTHESIS

Reduced efficiency of C fixation due to photorespiration under hot and dry environments acted as a driver in the evolution of the C_4 pathway. The C_4 photosynthetic pathway occurs in 7,500 of the world's 250,000 plant species and has evolved separately at least 66 times [31]. It consists of biochemical and anatomical modifications designed to concentrate CO_2 around Rubisco through the spatial separation of C uptake and fixation by Rubisco with the goal of suppressing photorespiration. C_4 photosynthesis typically involves two different cell types, the M and the BS cells, in a conformation termed the Kranz anatomy (Fig. 2).

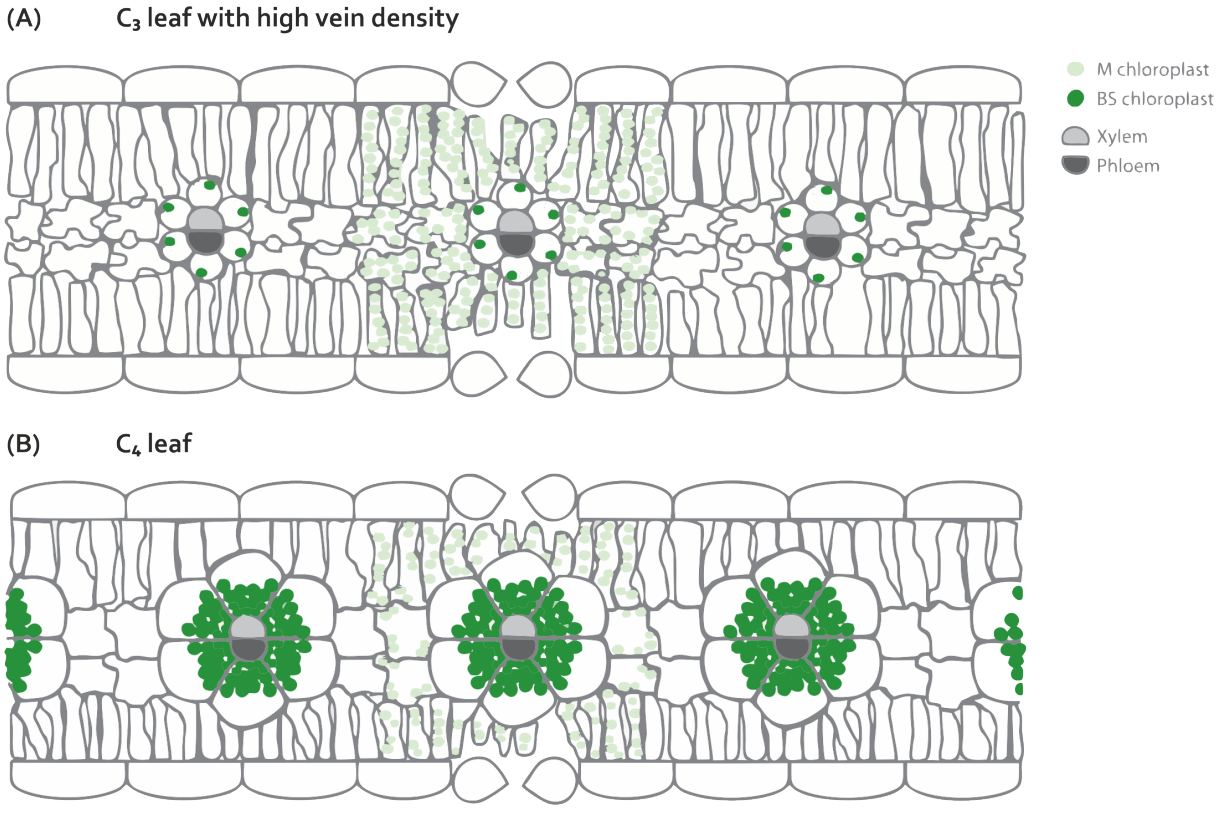

Figure 2 – Illustrations demonstrating the differences between C_3 and C_4 leaf structures. **(A)** Depiction of a C_3 leaf , representing a small BS cells with few organelles. **(B)** Presentation of a C_4 leaf with BS cells very large, reduced number of M cells relative to BS cells and BS chloroplasts are enlarged and centripetally positioned. Abbreviations: BS, bundle sheath; M, mesophyll. Adapted from [31]

The C_4 cycle involves the initial fixation of CO_2 in the form of bicarbonate in the M cells by Phosphoenolpyruvate Carboxylase (PEPC), resulting in oxaloacetate (OAA) that is converted to the transport metabolites malate or aspartate, which are both 4 C molecules, leading to the term "C_4". Malate or aspartate are then transported to the BS cells, where the C_4 molecule is decarboxylated releasing CO_2. The decarboxylation enzyme used can be either NADP-dependent Malic Enzyme (NADP-ME), NAD-dependent Malic Enzyme (NAD-ME), Phosphoenolpyruvate Carboxykinase (PEP-CK) or either a combination of NADP-ME:PEP-CK or NAD-ME:PEP-CK; the decarboxylation enzyme used determines the subtype of C_4 photosynthesis [32]. In the case of the NADP-ME subtype, the decarboxylation reaction produces Pyruvate, which is transferred back to the M cell where PEP is regenerated by Pyruvate, phosphate dikinase (PPDK). In NAD-ME and PEP-CK subtypes, the Pyruvate resulting from the decarboxylation reaction is transaminated and transported as Alanine. The released CO_2 in the BS cell is then re-fixed by Rubisco, which is located exclusively in the BS cells in C_4 plants (Fig. 3 (II)) [33]. This metabolism effectively concentrates the CO_2 from the intercellular air spaces of the leaf inside the BS cells. In addition to the gains resulting from the suppression of photorespiration, high CO_2 concentrations around Rubisco result in high rates of photosynthesis and increased efficiency in the use of H_2O and N resources [34].

Despite the advantages of the C_4 cycle, these gains can be offset by changing environmental conditions. To operate the C_4 cycle, extra ATP must be used when compared to the C_3 cycle. Under elevated CO_2 environments or at low temperatures, photosynthetic efficiency is greater in C_3 photosynthesis, making the C_4 cycle less efficient. This happens because of the combination of the reduction of photorespiration in the C_3 cycle in these conditions and the ATP costs associated with maintaining the C_4 cycle [26].

2.1.4 CAM PHOTOSYNTHESIS

While some plants evolved the C_4 pathway, in arid regions where plants experience severe H_2O stress and a Water-Use Efficiency (WUE) is a priority for plant survival, others evolved CAM photosynthesis. CAM photosynthesis is characterised by the temporal separation between C uptake from the atmosphere and fixation by Rubisco. When H_2O is limited, the guard cells close the stomata to prevent H_2O loss through evapotranspiration. However, this severs gas exchanges

between the leaf and the atmosphere, limiting CO_2 uptake by the plant. CAM plants overcome this by opening their stomata and taking up CO_2 primarily at night when the temperature is lower and relative humidity is higher, thus reducing H_2O loss. During this phase CO_2 is fixed by PEPC producing malate, which is stored in the vacuole overnight as malic acid. During the day the stomata are closed, the stored malate is decarboxylated and the resulting CO_2 is transported to the chloroplasts where it is fixed by Rubisco (Fig. 3 (III)). This metabolism greatly increases CAM plant's WUE, having a three- and six-fold higher WUE than C_4 and C_3 plants, respectively. The decarboxylation of malate also greatly increases CO_2 concentration around Rubisco, thereby reducing the increased photorespiration rates expected in high temperature environments [35, 36].

However, in the absence of H_2O limitation, CAM photosynthesis is outperformed by C_3 and C_4 photosynthesis due to its comparatively lower photosynthetic rates and higher energetic costs, causing many CAM plants to be slow growing and long-lived [37].

Interestingly, multiple lineages of CAM plants are aquatic. These plants evolved into CAM not because of H_2O limitation but rather C limitation in their environment. These plant habitats consist of temporary pools which experience elevated day/night C availability fluctuations. By opening their stomata during the night, the plants are able to take advantage of the elevated nighttime CO_2 levels, while preventing CO_2 diffusion during the day [38].

2.2 Energy metabolism

Reducing equivalents and energy are necessary to drive living processes [40]. Reducing equivalents are mostly provided as the pyridine nucleotides nicotinamide adenine dinucleotide reduced (NADH) and NADPH, while energy is provided by the carrier ATP. NADH and NADPH are generated through the reduction of nicotinamide adenine dinucleotide oxidized (NAD^+) and nicotinamide adenine dinucleotide phosphate oxidized ($NADP^+$), while ATP is generated through the phosphorylation of Adenosine Diphosphate (ADP). Energetic cellular metabolism operates on the turnover of these metabolites which act as currency to fuel some metabolic processes and are regenerated through others.

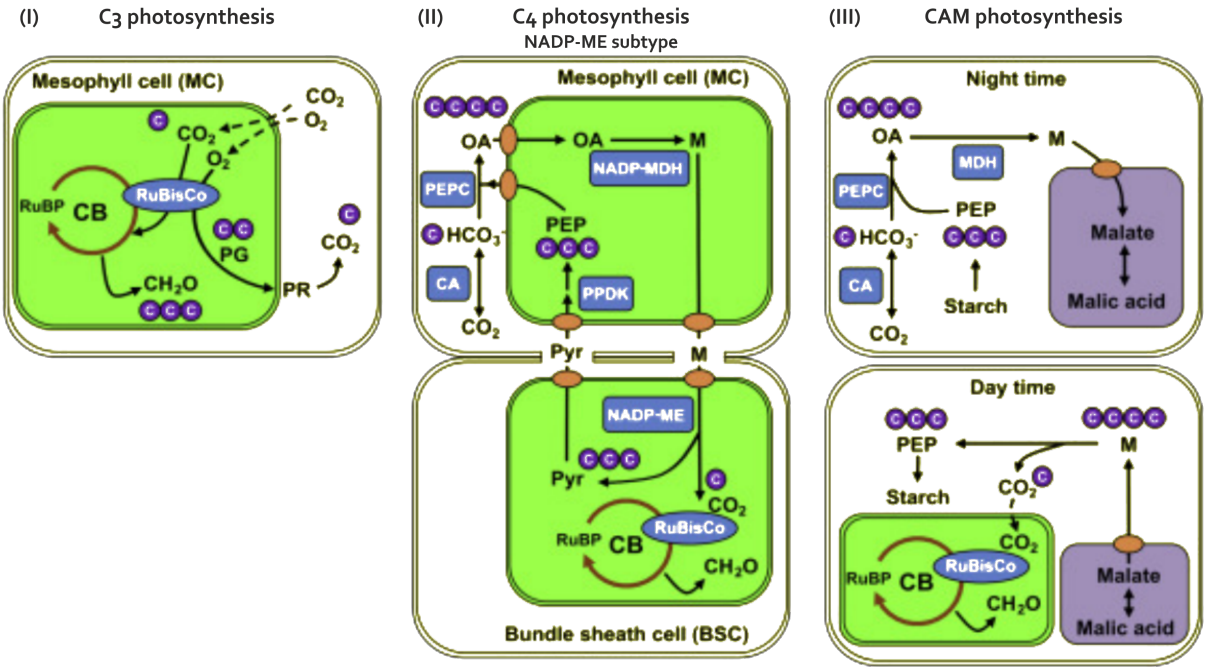

Figure 3 – Schematic representations of C_3, C_4 and CAM photosynthesis. (I) In C_3 photosynthesis Rubisco demonstrates both carboxylase and oxygenase activity, leading to the formation of PG which undergoes photorespiration; (II) During C_4 photosynthesis CO_2 is initially fixed as malate in the MC and then transported to the BSC. There it is converted into Pyr by NADP-ME which concentrates CO_2 around Rubisco. (III) CAM photosynthesis allows for fixation of CO_2 during the night and the resulting malate is stored in the vacuole. During the day the stored malate is released and decarboxylated, releasing CO_2 for Rubisco carboxylase activity and regenerating PEP. Chloroplasts are represented in green and vacuoles in lilac. Abbreviations: CA, carbonic anhydrase; M, malate; MDH, malate dehydrogenase; ME, malic enzyme; OA, oxaloacetate; PEP, phosphoenolpyruvate; PEPC, phosphoenolpyruvate carboxylase; CB, Calvin-Benson-Basham cycle; PG, phosphoglycolate; PR, photorespiration; Pyr, pyruvate; PPDK, pyruvate phosphate dikinase. Adapted from [39]

The generation of these compounds occurs in different pathways across different subcellular compartments [41]. As overviewed in Chapter 2.1, NADPH and ATP are generated under illuminated conditions during the light reactions of photosynthesis. These products drive CO_2 fixation into organic molecules in the CBB cycle, and more ATP and reducing power need to be generated and made available in the cytosol to satisfy cellular demand [42]. Additional ATP generation occurs in the cytosol through glycolysis and in the mitochondria through oxidative phosphorylation [43]. Similarly, reducing equivalent generation also occurs as NADH in the cytosol through glycolysis and in the mitochondria through the Tricarboxylic Acid (TCA) cycle; and as NADPH in the plastid and cytosol through the pentose phosphate pathway (Fig. 4).

The primary role of NADH is to transfer electrons from the oxidation of substrates into the mitochondrial electron transport chain to generate the proton gradient necessary for ATP syn-

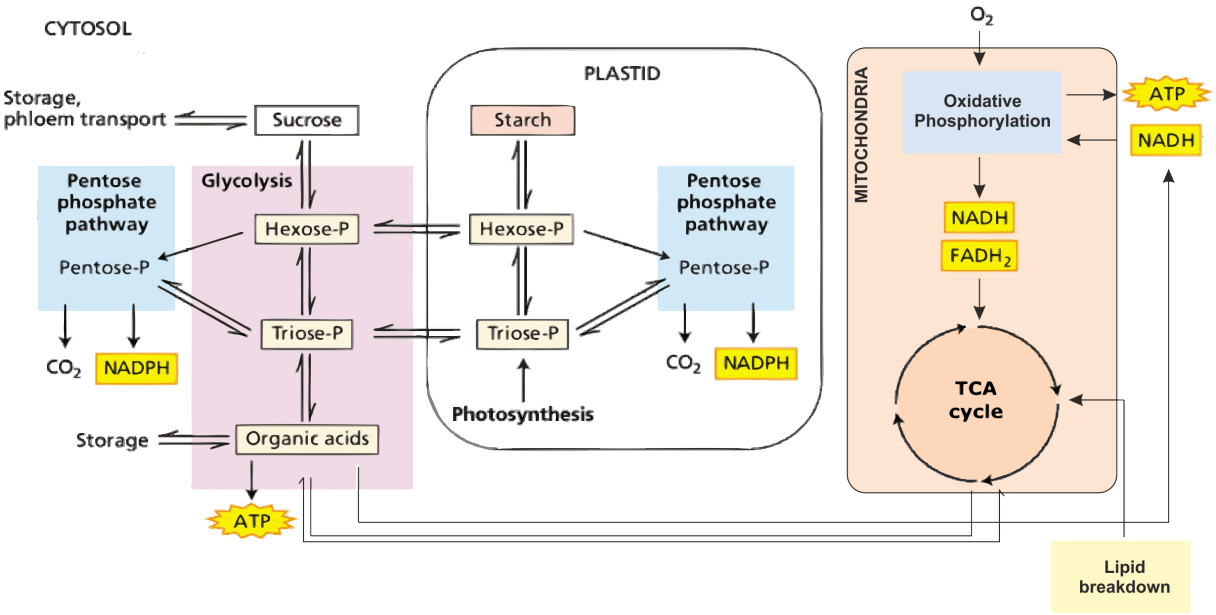

Figure 4 – Schematic overview of plant respiration. Substrates for mitochondrial respiration are priorly generated by other metabolic processes. Glycolysis and the pentose phosphate pathways convert sugars, in the form of sucrose to organic acids, generating NADH or NADPH and ATP. The organic acids are further oxidized in the TCA cycle, and the NADH and flavin adenine dinucleotide ($FADH_2$) are produced there to provide energy for ATP synthesis in the oxidative phosphorylation pathway. Adapted from [44]

.

thesis. On the other hand, NADPH mostly provides a supply of reducing power for biosynthesis, oxidative stress responses and the maintenance of thiol redox networks [45].

Additionally, the pyridine nucleotides serve not only a central role in energy metabolism [46] but also have roles in development [47], signalling [48], reactive oxygen, reactive N species and biosynthesis [49], gene expression [50], immunity [51], and post-harvest metabolism [52].

In addition to plant respiration, the photosynthetic electron transport chain may switch between linear electron transport to cyclic electron transport in order to provide additional ATP to satisfy cellular needs [53]. In this chapter, we will detail the activity of the photosynthetic electron transport chain and its variations with regard to its impact on plant metabolism.

2.2.1 Linear electron transport

The light reactions of photosynthesis are composed of chemical processes carried out by four major protein complexes: PSII, the cyt b6f, PSI, and ATPase [18]. Light capture during

photosynthesis occurs at two spatially separated reaction centres: PSI and PSII, that function in tandem. The chlorophyll within these reaction centres absorbs light at different wavelengths, with PSI absorbing maximally at 700 nm and PSII absorbing at 680 nm. PSI produces a strong reductant, capable of reducing $NADP^+$ and a weak oxidant, while PSII produces a strong oxidant (used to oxidize H_2O) and a weak reductant. An electron transport chain connects these two centres in a Z (zigzag) scheme (Fig. 5). The cyt b6f receives electrons from PSII and delivers them to PSI (participating in the electron transport chain). Both PSII and the cyt b6f pump protons into the lumen of the thylakoid, making them available for ATPase, which produces ATP as protons are pumped through it from the lumen into the stroma [44].

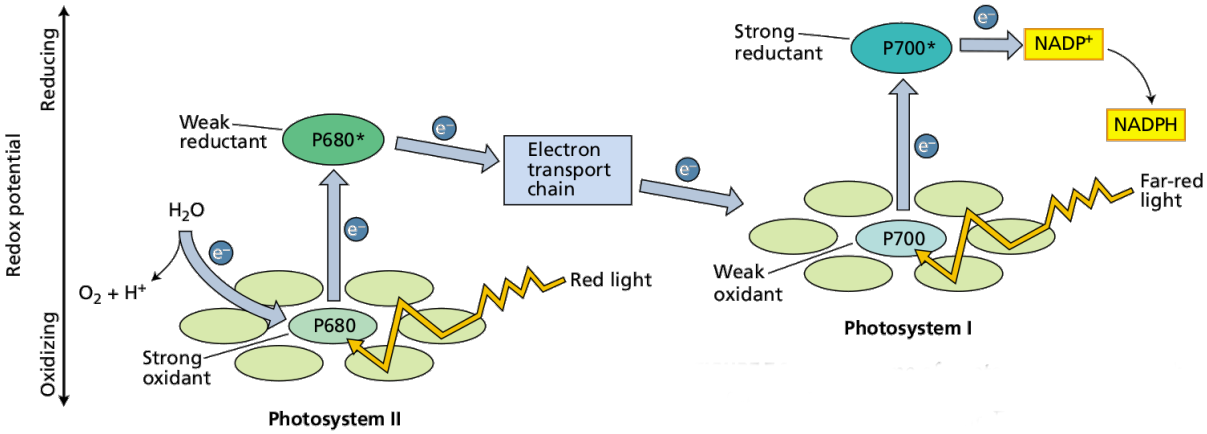

Figure 5 – Z scheme of photosynthesis. Red light is absorbed by PSII, producing a strong oxidant and a weak reductant, while PSI absorbs far-red light producing a weak oxidant and a strong reductant. The oxidant produced by PSII is used to oxidize H_2O, while the reductant produced by PSI is used to reduce $NADP^+$. Adapted from [44].

In this series of reactions, the electron donor is H_2O, which PSII oxidizes according to Equation 2 [54].

$$2\,H_2O \rightarrow O_2 + 4\,H^+ + 4\,e^- \tag{2}$$

From two H_2O molecules, four electrons are removed, generating an O_2 molecule and four hydrogen ions which are released into the lumen. These electrons are then transferred into plastoquinone (PQ), yielding the reduced compound plastohydroquinone (PQH2), which in turn transfers those electrons into the cyt b6f. Through this complex, electrons are transferred to plastocyanin (PC) in a cyclic process termed the Q cycle, resulting in the regeneration of PQ and the transport of protons across the thylakoid membrane into the lumen. PC then reduces

the PSI. Overall, for every two electrons delivered to PSI, four protons are transported thylakoid membrane into the lumen, two PQH2 are oxidized to PQ and one PQ is reduced to PQH2. Within PSI electrons are transferred to the small soluble protein ferredoxin (Fd). The final acceptor of this chain is $NADP^+$, which is reduced by the membrane-associated flavoprotein Ferrodoxin-NADP+ Reductase (FNR) to NADPH, thereby completing the linear electron transport (Fig 6) [39].

2.2.2 Cyclic electron transport

Electron flow through the cyt b6f is coupled with proton pumping into the lumen, which is in turn used for ATP generation. Under certain conditions, electron flow can cycle back to the cyt b6f through the reduction of PQ instead of the reduction of $NADP^+$ by FNR. This cyclic electron flow results in additional ATP production, but production of no reducing equivalents (NADPH). In addition, it is thought to play a role in plant photoprotection responses and regulating electron transfer at the cyt b6f [55].

Four distinct pathways for cyclic electron flow are described, diverging at the PQ reductase step, where electrons from PSI are transferred into the PQ pool. Maize thylakoids contain a type 1 NADPH dehydrogenase (NDH) complex, which participates in cyclic electron transport, by reducing PQ while pumping additional protons to the lumen [56]. This pathway and other alternatives are illustrated in Figure 6.

Cyclic electron transfer has been shown to play a role in energy balance in C_4 metabolism [57]. Maize, a mostly NADP-ME C_4 species, shows a strong BS expression of NDH protein complex accompanied by reduced BS PSII activity [58], while both NDH and PGR5 were found overexpressed in NAD-ME C_4 compared to C_3 and C_3-C_4 intermediate species of *Flaveria* [59]. Due to the extra ATP requirements of the C_4 cycle, it is theorized that this can be met by increased cyclic electron transport in BS cells. More specifically for NADP-ME species, the net transfer of NADPH from M to BS cells implies a reduced requirement for linear electron transport to produce NADPH in the BS chloroplast [60].

The exact environmental and metabolic conditions that lead to cyclic electron transport regulation are still an active area of research, particularly with regards to C_4 photosynthesis [61].

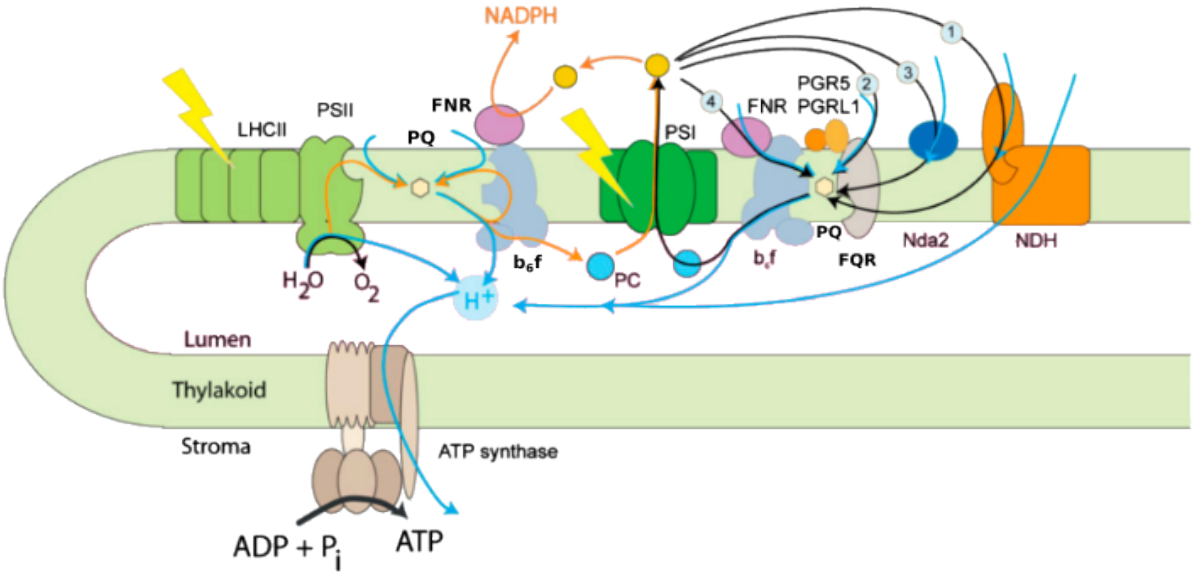

Figure 6 – Representation of linear and cyclic electron transport. Orange arrows indicate linear electron transport, black arrows cyclic electron transport and blue arrows indicate proton movement. Four different pathways for cyclic electron transport are shown: 1) NDH complex; 2) Fd-PQ oxidoreductase (FQR); 3) type 2 NADPH:PQ oxidoreductase (Nda2); and 4) cyt b6f with the possible involvement of FNR. Adapted from [55]

2.3 Nitrogen metabolism

N is an essential component for the biosynthesis of amino acids and proteins, nucleic acids, cell wall components, hormones, vitamins and others [62]. Plants require an uptake of N from the environment during autotrophic growth, which is available either as nitrate (NO_3^-) or NH_4^+. N is uptaken directly from the soil through the roots or from the air through symbiosis with N-fixing bacteria in the rhizosphere. However, the majority of N uptake by plants is done via the soil in the form of NO_3^-, since NH_4^+ is oxidised to NO_3^- by nitrifying bacteria. An exception to this are flooded or acidic soils, in which NH_4^+ is the predominant N source [63]. Assimilation of NO_3^- can occur either in the roots or the leaves. Root assimilation occurs mainly at an early growth stage and also in many woody plants and some legumes. Leaf assimilation occurs in fully grown herbaceous plants [64].

In root cells, N transported into the roots can be stored in vacuoles, used for the synthesis of the amino acids glutamine and asparagine, or sent into the xylem in order to be assimilated by the leaves [65]. In C_3 plant leaves under photoautotrophic conditions, NO_3^- is uptaken into

the M cells, where it is reduced to nitrite (NO_2^-) by the action of Nitrate Reductase (NR) in the cytosol, with NADH as a reductant. NO_2^- is toxic and all NO_2^- formed by this reaction is quickly transported to the chloroplast where it is reduced to NH_4^+ by Nitrite Reductase (NiR), using Fd supplied by PSI as an electron donor [66]. The produced NH_4^+ is then transferred into glutamate at the expense of ATP by Glutamine Synthase (GS), forming glutamine. Glutamine is then converted back to glutamate via Glutamate Synthase (GOGAT), which makes glutamine react with one molecule of α-ketoglutarate to form two molecules of glutamate, using Fd as a reductant (Fd-GOGAT). The organic acid α-ketoglutarate acts as an important intermediate in the TCA cycle and acts here as a C skeleton for N assimilation. Another form of GOGAT also exists in plants, which used NADH as a reductant (NADH-GOGAT) [67]. The activity of GS and GOGAT operate in a cyclic way and are collectively designated as the GS-GOGAT cycle. Glutamine and glutamate then serve as the precursors to generate other biomolecules containing N [68].

C_4 plants differ significantly from C_3 plants in the compartmentalization of N metabolism and also in N use efficiency [69]. C_4 species display a greater N use efficiency than C_3 species, which is speculated to be connected with the lower amounts of Rubisco required for C fixation due to the C concentration mechanism, and the reduced need for photorespiratory N recycling. In addition, C_4 plants also segregate the enzymatic mechanism of N assimilation in a cell-specific way, between the BS and the M cells [70]. NO_3^- or NH_4^+ are generally uptaken by the BS cell through the xylem vessels. In maize, NR and NiR are exclusively present in the M cells, while the GS-GOGAT cycle operates in both BS or M cells, or exclusively on the BS cell. Additionally, GDC, a key photorespiratory enzyme located in the mitochondria whose activity leads to the production of NH_4^+, is exclusively located in the BS cell of C_4 plants [71]. In the event of oxygenase activity by the BS Rubisco, the NH_4^+ released by the subsequent C_2 cycle activity would be re-assimilated by the GS-GOGAT cycle in the BS [72] (Fig. 7).

Despite this, several questions regarding N assimilation are not completely answered. It is not understood what advantages the cell-specific distribution of N assimilation enables in C_4 plants, nor how leaf anatomical variation impacts this distribution [73]. Thus, studies expanding on N assimilation in C_4 may help us shed more light on these subjects and contribute to a greater understanding of future bio-engineering strategies of C_4 metabolism and N fixation.

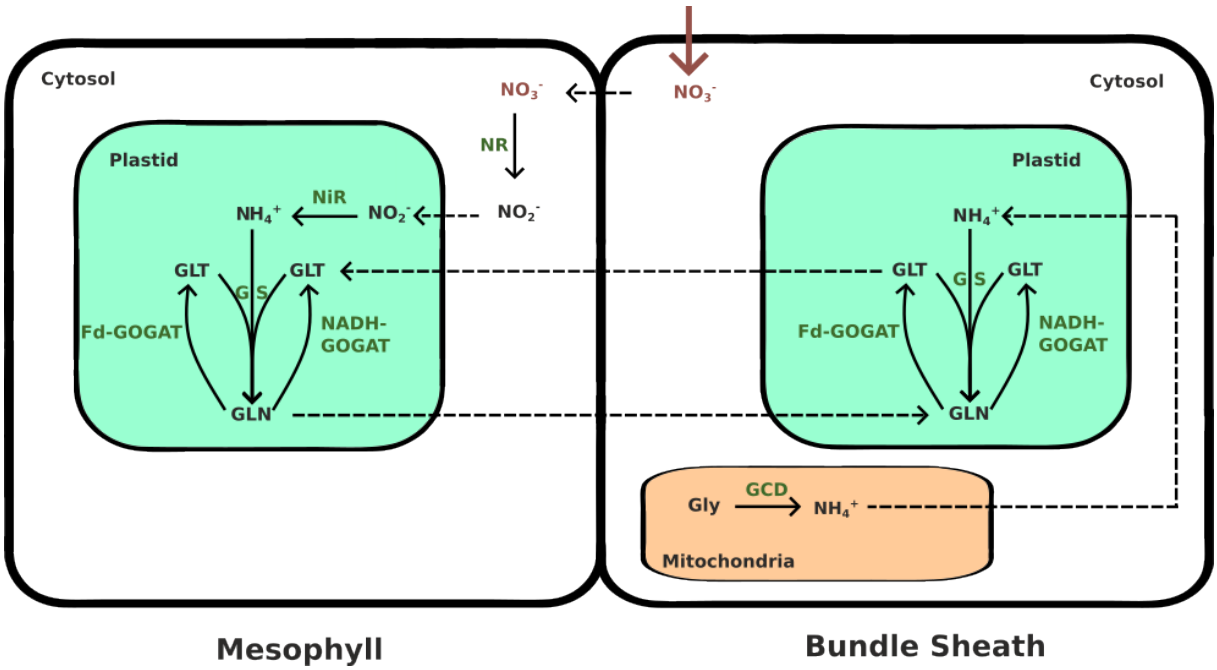

Figure 7 – Schematic of N uptake in a maize leaf. NO_3^- is uptaken by the BS from the xylem and is transported to the M cell where it is reduced to NH_4^+ by the activity of NR in the cytosol and NiR in the plastid. The NH_4^+ enters the GS-GOGAT cycle and is converted into glutamate and glutamine. For the GOGAT reaction, Fd or NADH can be used as reductants. Glutamine can then be transported to the plastid of the BS cell, where it contributes to the assimilation of NH_4^+ released by GDC during the C_2 cycle. Transport reactions are indicated in dashed arrows. Abbreviations: NO_3^-, nitrate; NO_2^-, nitrite; NH_4^+, ammonium; GLT, glutamate; GLN, glutamine; Gly, glycine; NR, nitrate reductase; NiR, nitrite reductase; GS, glutamine synthase; GOGAT, glutamate synthase; GDC, glycine decarboxylase, Fd, ferredoxin. Adapted from [72]

2.4 Constraint-based modelling

One of the greatest achievements in systems biology is the use of computational models to predict biological activity, using methods such as COnstraints-Based Reconstruction and Analysis (COBRA). Due to the increased availability of biological data, several databases exist detailing biochemical and genetic components that comprise cellular activity, including metabolic pathway information such as genes, proteins, reactions and the relationships between these components [74]. Through the data stored in these databases, it is possible to generate network reconstructions of cellular metabolism based on genome annotation, biochemical characterisation, and scientific literature. Such a network can, for example, represent biochemical reactions known or predicted in a given organism. Representing the metabolic reactions of a given cell, alongside genetic context and gene genomic location leads to the construction of a

Genome Scale (GES) network. Smaller subsections of metabolism may be used when building the models, leading to the construction of more specific large or small–scale models. These metabolic networks can be mathematically represented and used to generate computational predictions of biological functions [15].

The mathematical representation of such a network can be accomplished through the depiction of the stoichiometric coefficients of each reaction in the form of a numerical matrix (S), of size m×n, in which every row represents a unique compound (m compounds), and every column represents one reaction (n reactions), while the flux through all the reactions in the network is represented by a vector (v). Typically, there are more reactions than metabolites in the model ($n > m$) making the system underdetermined, leading to many possible solutions [75].

In CBM, constraints are represented as equations that represent balances or inequalities that impose bounds on flux values. The matrix S imposes mass balance constraints, ensuring that the total amount of any compound produced in the network must be equal to the total amount consumed at steady state. Each reaction is also given a lower and upper bound, which set the minimum and maximum flux values, respectively. Constraining creates a space of flux solutions, in which each point can be mathematically represented as a flux distribution listing all flux values for that point (Fig. 8) [76].

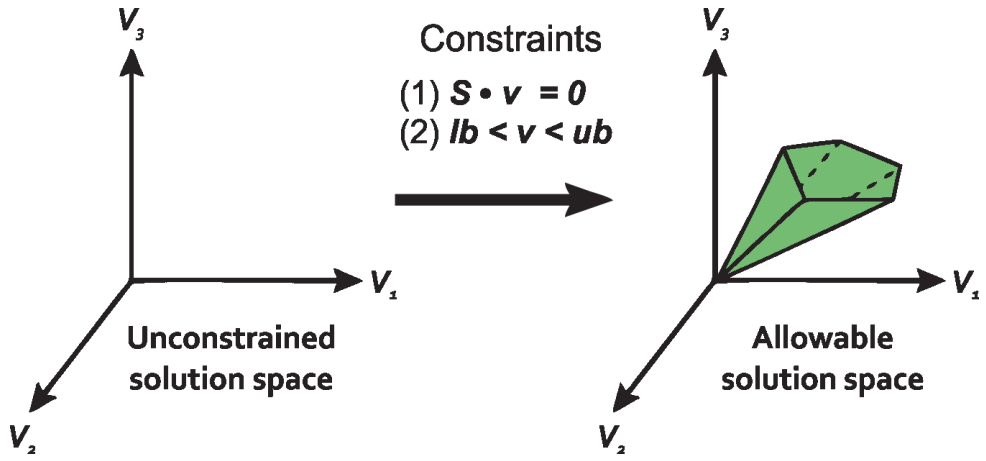

Figure 8 – Conceptual basis of constraint-based modelling. When no constraints exist on the solution space, the flux distribution may occur anywhere in the solution space. Through applying mass balance constraints (1) and constraints on fluxes upper and lower bounds (2) a constrained solution space is defined. Adapted from [77].

2.4.1 Flux balance analysis

Although the imposed constraints define a range of possible flux solutions, one may be interested in finding a specific point in that space, for instance, the maximum growth rate and corresponding flux distribution. This optimal point can be found using Flux-Balance Analysis (FBA) [77]. In FBA, it is assumed that biological systems optimise a given objective function $Z = c^T v$, which can be any linear combination of fluxes, where c is a vector of weights indicating how much each reaction contributes to the objective. The goal of FBA is to find a flux distribution that either minimises or maximises Z.

In Equation (3), the FBA linear problem is represented, starting with the objective, in this case, the maximisation of a given objective function; this is followed by assuming the flow of metabolites in the network to be at a steady state; finally, network fluxes are further constrained between two bounds. From a biological perspective, this objective function can take the shape of the maximisation of ATP production or maximisation of the flux through a specific biomass reaction. This biomass reaction corresponds to a sink reaction consisting of the weighted sum of metabolites used in cellular growth. These weights are typically derived from experimental measures and are represented as ratios in the reaction stoichiometry.

$$\begin{aligned} &max(c^T \cdot v) \\ &\text{subject to } S \cdot v = 0 \\ &lb < v < ub \end{aligned} \tag{3}$$

Through solving the described linear programming problem, a set of optimal steady-state flux distributions that satisfy the given constraints is reached. The pipeline for FBA analysis is exemplified in Fig. (9).

2.4.2 Parsimonious flux balance analysis

In addition to FBA, other extensions of this methodology can also be used to obtain optimal solutions. One such method is a variation of FBA termed parsimonious enzyme usage FBA (pFBA) [78]. In pFBA, the underlying assumption is that cells have a limited total enzymatic

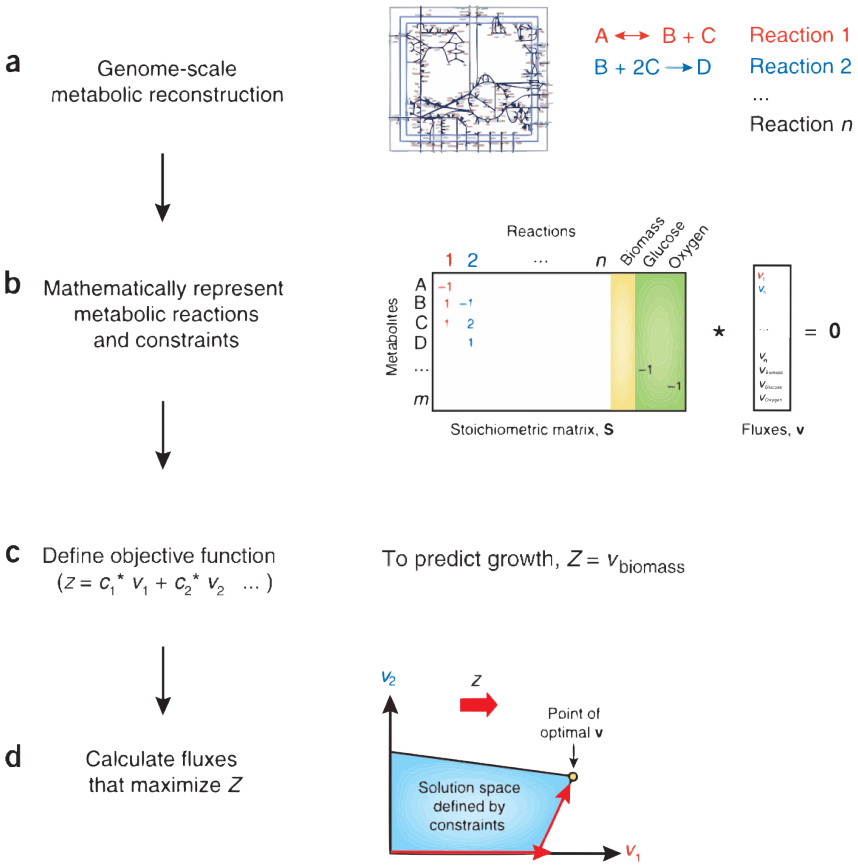

Figure 9 – Schematic representation of the formulation of an FBA problem. **(a)** To perform FBA, one must first build a metabolic network reconstruction consisting of a list of stoichiometrically balanced biochemical reactions; **(b)** The reactions are then converted into the stoichiometric matrix (S). The flow of metabolites is assumed to be at a steady state as given by $S \cdot v = 0$; **(c)** To solve the system of equations, an objective function (Z) is defined, in this case, maximisation of biomass; **(d)** Linear programming is used to identify the flux distribution that maximises or minimises the objective function within the space of feasible fluxes (blue region). The thick red arrow indicates the direction of increasing Z, while the thin red arrows depict the process of linear programming, culminating in the identification of an optimal point. Adapted from [77].

capacity and have therefore evolved to minimise the costs for the synthesis of enzyme and membrane transporters that support cell growth and maintenance [79].

These assumptions are mathematically approximated by employing FBA to optimise the objective function, followed by minimising the net metabolic flux through all reactions in the network. The latter is obtained through the addition of a constraint to minimise the sum of the absolute flux values to the FBA linear problem, creating a two-step linear problem. Therefore, pFBA finds the subset of genes and proteins that may contribute to the most efficient metabolic network topology to a given set of constraints. This methodology allows the obtention of predicted

flux distributions which are more closely correlated to in vivo distributions, as described through comparison with omic data [80].

2.4.3 Flux variability analysis

The methods discussed above allow the computation of the optimal flux distribution in the flux solution space that optimises a given objective function. However, these flux distributions may not be unique. For any optimal flux distribution, there may exist alternate optimal solutions defining a region in the flux solution space that generate the same objective function value via different flux distributions, while satisfying all the imposed constraints. The occurrence of these alternative distributions stems from the flexibility of metabolism, namely the existence of several metabolic pathways that can lead to the production of the same metabolites, creating redundancy in the metabolic network [81].

One way to approach this issue is through another COBRA method defined as Flux Variability Analysis (FVA). FVA is used to find the minimum and maximum flux for reactions in a given network. It also allows for the exploration of these parameters under suboptimal conditions, e.g., 80% of maximal possible biomass production. After solving equation (3), FVA solves two optimisation problems for each flux of interest. The linear programming problem for FVA is shown in equation 4, where $Z_0 = w^T v_0$ is an optimal solution to equation 3; additionally γ controls whether the analysis is performed on suboptimal network states ($0 \leq \gamma < 1$) or on the optimal state ($\gamma = 1$). The solution to equation 3 determines the upper and lower bounds of every reaction flux that will result in the same value for the original objective function (Fig. 10) [82].

$$\begin{gathered} max_v / min_v \, v_i \\ \text{subject to } S \cdot v = 0 \\ w^T v \geq \gamma \, Z_0 \\ lb < v < ub \end{gathered} \tag{4}$$

The computed flux boundaries allow for confirmation of flux variability throughout the network, with these findings translating into alternative optimal flux distributions.

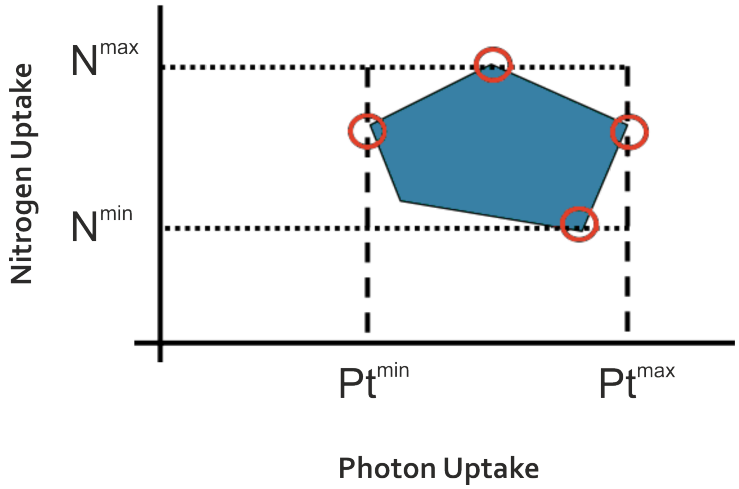

Figure 10 – Schematic of the optimal solution space and FVA results. The blue polygon represents the region where the objective function can take on the same optimal value, and the red circles represent maximum and minimum flux values that allow the optimal objective function value, which can be determined using FVA. N and photon uptake reactions are used as examples for FVA computation. Adapted from [81].

2.5 Modelling plant metabolism

2.5.1 Plant metabolic models

In the past decade, there has been a rapid increase in the number of sequenced plant genomes [83]. Data from public databases such as Kyoto Encyclopedia of Genes and Genomes (KEGG) [84], PlantSEED [85] and The Plant Metabolic Network Database [86], provide organism-specific information on genes, enzymes, reactions and metabolites which can be implemented in reconstructing plant metabolic network models. Such stoichiometric models exist for different plant species and can be classified as ”core” models, restricted to the well-known and conserved pathways of the central C metabolism and GES models, which contain all the reactions catalysed by the enzymes encoded in an annotated genome [87].

Most stoichiometric models for plant metabolism consider only one cell type. The first developed models considered primarily leaf metabolism, using such models to study both autotrophic and heterotrophic metabolism. However, more recently, multi-cell models are being built, representing multi-tissue and whole-plant level networks. In general, these models serve as powerful tools to study the metabolic capacities of single cells [88]; guide systems-level

metabolic pathway analysis [89]; interactions between the M and BS cells in C_4 photosynthesis [17]; interactions between different tissues in developing seeds [90]; explore whole-plant systems represented by connected leaf, stem, and root cell models [90]; whole-plant diel models [91]; and rhizobial symbiosis in legumes [92], among others.

However, there are several challenges to plant network reconstruction. There is a lack of detailed experimental information available for genome annotation, even for intensely studied organisms. For *Arabidopsis thaliana*, the main model for plant biology studies, an estimated 21% of enzymes are missing direct experimental evidence [93]. In addition, enzyme promiscuity, which is prevalent in plant specialised (secondary) metabolism, makes it difficult to accurately define stoichiometry in metabolic networks. Lastly, in existing databases, there are still knowledge gaps regarding metabolite intracellular transport and enzyme subcellular location. These limitations may force modellers to adopt either conservative or non-conservative approaches. The former involves curating pathways in order to only include information backed by strong evidence [94]; the latter involves filling the knowledge gaps with related data such as known orthologs from related or any species, in a process termed gap-filling [95]. Despite these challenges, the number of available plant models has dramatically increased over the last decade. In 2020, Clark et al. reviewed the published plant genome-scale models and found 35 published models for 19 plant species [96].

Töpfer reviewed in 2021 the existing flux-balance models of leaf metabolism [16]. They were divided into the models investigating the leaf metabolic responses through constraining environmental variables, such as light, CO_2, O_2 and nutrient uptake exchange reactions; and into data-driven models, integrating omics data to constraint reaction fluxes. In the latter case, data was collected from leaf material exposed to different environments. Additionally, these studies were organised according to modelling either biotic or abiotic interactions. These included species-specific leaf models for rice [97, 98] , Arabidopsis [99, 100], maize [101–103], tomato [104], potato [105], Flaveria genus [106]; and generic models for CAM [107], C_4 [17] and C_3-CAM photosynthesis [35].

2.5.2 Context-specific models

Network reconstruction at GES captures all reactions in all tissues, whereas context-specific models seek to capture the relevant reactions in a particular tissue and context. Plant metabolism is dynamic, changing from tissue to tissue and in response to the environment [108]. Much of plant secondary metabolism, for example, is induced by abiotic or biotic stress. In a given cell, gene expression dictates which pathways can be used at any time point [109]. The construction of such context-specific models can be achieved through the integration of omics data, which are used to constrain reaction fluxes in a GES model. Methods such as PROM [110], iMAT [111], MADE [112], GIMME [113], AdaM [114] and E-flux [115] are examples of frameworks used to integrate transcriptomics data as flux constraints in stoichiometric models. In addition, multi-omics approaches are also being developed by mapping gene-protein-reaction relationships, allowing for the joint integration of transcriptome, proteome, and metabolome data [116]. The abundance of available data in pathway databases makes it easier to build increasingly complete and specific models. However, the question of the practicality of larger networks arises. For example, in an Arabidopsis GES model [117], only a fraction of total reactions carried flux during after FBA simulations. This happened because only a subset of the network was required to synthesise the main biomass components and account for maintenance-associated energetic costs. Furthermore, both the number of active reactions and the reactions themselves were similar to FBA models of primary metabolism [109]. As such, to model photosynthetic pathways, a core model of central metabolism is sufficient to simulate heterotrophic and autotrophic growth.

2.6 Leaf anatomical constraints

C_3 plants evolution into C_4 plants is accompanied by several modifications of leaf anatomy [118]. Leaf architecture of C_4 plants is collectively designated of Kranz anatomy, with one of the most common phenotypes presented above in Fig.2. Despite this, there is a considerable anatomical variation in the Kranz syndrome among C_4 species, resulting from convergent evolution from several plant lineages [119]. There are four essential anatomical requirements for C_4 photosynthesis: I) Two distinct cell types are arranged so that atmospheric gases reach

the M cell more easily than the BS cell. The M cell houses PEPC, while the BS cell houses the CBB cycle; II) The two cell types must be in close contact to allow the rapid exchange of metabolites; III) The cell where the CBB cycle is housed (BS cell) must occupy a large enough fraction of the leaf to accommodate a significant amount of chloroplasts, and IV) Chloroplasts must be abundant in the CBB cycle cell [120–124]. Prevention of atmosphere contact with BS cell is essential to photorespiration [34]. Close contact between the cell types, coupled with the abundance of plasmodesmata, allows the fast exchange of C_4 acids (malate or aspartate) from theM to the BS. This exchange, together with the transport of Phosphoenolpyruvate (PEP) or pyruvate back to the M cell, enables the carbon concentration mechanism [125]. The increase in BS cell tissue ratio in C_4 plants compared to C_3 plants is connected with the need for a larger number of chloroplasts to house Rubisco, whose activity is no longer present in the M chloroplasts. This increase in BS tissue can be achieved by an increase in BS size or number, depending on the C_4 species [119].

Within these constraints there is a considerable anatomical variation, encompassing mitochondria and chloroplast size and abundance, the position of those within the BS cells and the presence of suberin in the walls of BS cells [27, 126, 127]. Variation also occurs in organelle function depending on C_4 subtypes, with, as an example, PSII being deactivated in NADP-ME C_4 plants chloroplasts while this is not the case in NAD-ME subtype C_4 plants [128]. The NADP-ME subtype allows the transport of NADPH from M chloroplast linear electron transport to the BS in the form of malate and through the triose phosphate-3-phosphoglycerate shuttle. This reduces the need for BS chloroplast to produce NADPH and leads to their specialisation in cyclic electron transport and CBB cycle activity. In addition, several NADP-ME species, such as Maize, display agranal BS chloroplasts. In agranal chloroplasts, thylakoids do not form grana and require higher light intensities for PSII activation, thereby reinforcing maize BS chloroplast's specialization in cyclic electron transport [129].

Due to Kranz anatomy, BS cells are shaded by their surrounding M cells, resulting in lesser light penetration to the former [61]. It is postulated that the relative area ratios of BS:M tissue ratio affects the degree of shading of BS cells, and therefore the light uptake by BS chloroplasts. These changes in light absorption alter BS light-dependent energetic metabolism and therefore influence the energetic exchanges of the C_4 cycle as a whole. As with other traits related to Kranz anatomy, there is a suite of variations of BS:M tissue ratio compatible with C_4 metabolism,

spread over several C_4 species [130]. It follows that variations in this ratio will thereby affect the energy metabolism inherent to the C_4 cycle, and may contribute to observed differences in the cell-specific distribution of metabolic processes in these species [131].

Despite the extensive use of CBM to model C_4 metabolism, none have considered the effect of differential BS:M tissue ratios or quantified its metabolic impact through the analysis of predicted flux distributions. We hypothesise that by adding such anatomical constraints to a CBM framework, more accurate flux predictions may be obtained, particularly with regard to C_4 leaf energetic metabolism.

3

METHODS

In this section, I explain how we built the models used in our analysis, the specific constraints utilized and how the anatomical constraints were implemented into the model. In the end, I discuss methodologies used to perform the flux simulations. All the code used can be found on the following link: https://github.com/Toepfer-Lab/Anatomical_Constraints_C4.

3.1 MODEL BUILDING

The models were built and implemented using Python with the COnstraints-Based Reconstruction and Analysis for Python COnstraints-Based Reconstruction and Analysis for Python (COBRApy) package for model visualization and manipulation [132]. COBRApy is a python package for CBM that allows the implementation of COBRA methods. Additionally, species-specific biomass compositions were added to the models. The developed models correspond to large-scale growing leaf cell models that are capable of both autotrophic and heterotrophic metabolism. These models encompass reactions from plant primary metabolism, which are charge- and proton-balanced by considering molecular protonation states [107]. Plant primary metabolism encompasses all reactions needed for plant growth and development and is highly conserved in higher species [133]. In order to simulate a growing leaf, the objective function was defined as the maximization of biomass production.

On one side, architectural and external contains were added, consisting of adding missing reactions, constraining metabolite uptakes reactions into the model and parameterising exchanges between the cell types. On the other, internal constraints were added in order to

ensure either a C_4-specific flux distribution or to add specific constraints pertaining to maize metabolism. These constraints are further detailed below.

3.1.1 MODELS

The initial model was a generic C_3 model of plant central carbon metabolism provided by the Sweetlove group [134]. C_4 photosynthesis evolved from C_3, making all C_4 enzymes already present in the C_3 model [133]. This model is composed of 861 metabolites and 896 reactions. The model is further compartmentalised into 12 sub-cellular compartments, including the plastid, peroxisome, vacuole, cytosol, mitochondria, and endoplasmatic reticulum (Fig. 11). Pathway information for 208 pathways is also available for model reactions.

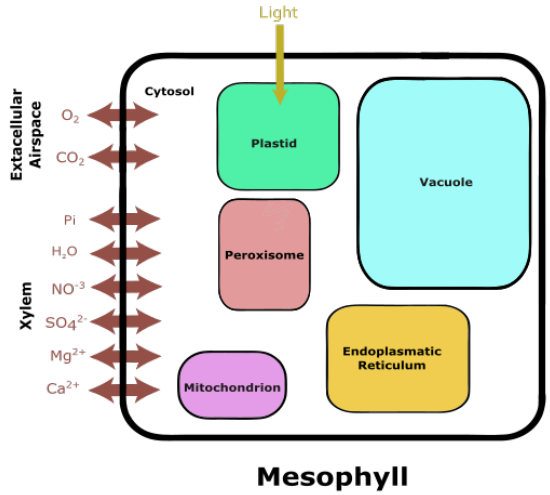

Figure 11 – Schematic representation of the C_3 one-cell model. The model contains several subcellular compartments which possess their own reactions and transport metabolites through the cytosol. The model can import and export metabolites from the extracellular environment to the cytosol through the use of exchange reactions.

We used the pipeline described by [17] to generate our maize C_4 leaf model. The model-building process involved the duplication of the C_3 generic model and the connection of the two network copies with transporters of cytosolic metabolites (Fig. 12). The initial capture of carbon occurred as CO_2 in the M cell which was then transported to the BS cell. Here, carbon was refixed by Rubisco in the CBB cycle, enabling growth. The biomass composition was obtained

from [85, 101, 135], and encompasses proteins, carbohydrates, cell wall constituents, lipids and soluble metabolites. The flux unit used in the model is μmol m^{-2} s^{-1} corresponding to the amount of flux through a reaction (μmol) by a given area (1 m^2) in a given timeframe (1 s).

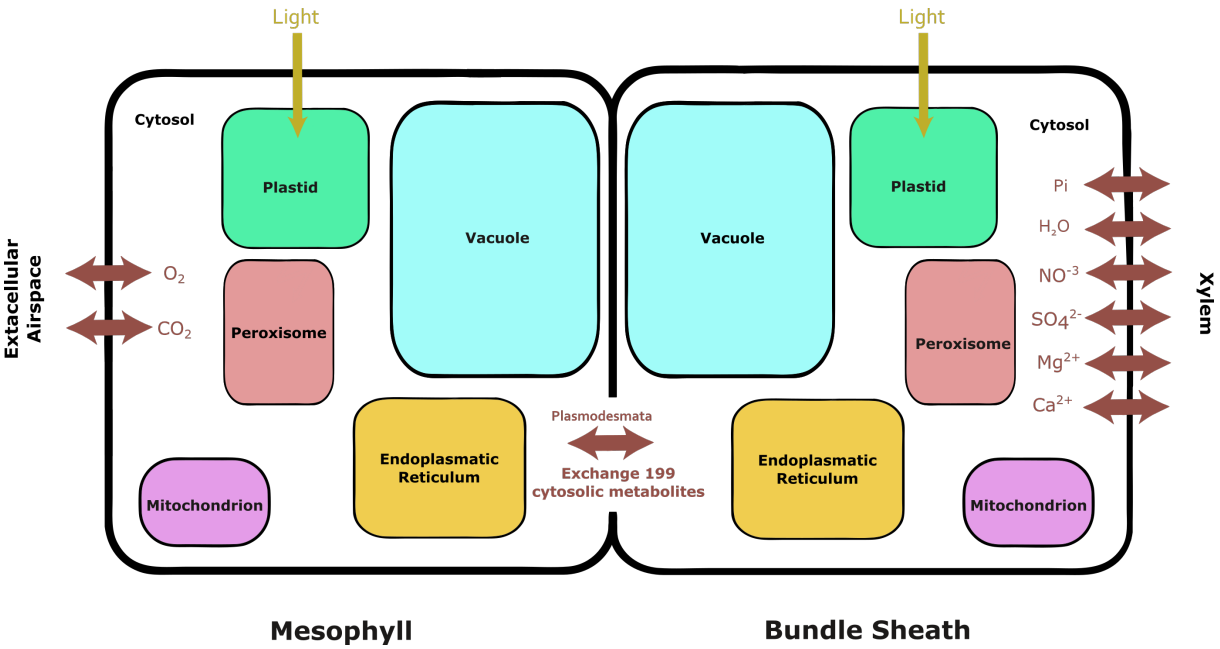

Figure 12 – Schematic representation of the C_4 two-cell model. The M cell is allowed to exchange gases with the extracellular airspace, while the BS exchanges inorganic and organic molecules with the xylem. Cytosolic exchange reactions are added between the models allowing carbon to be supplied to the BS cell where the CBB cycle occurs. This allows the production of starch, sugars and amino acids which are then exported through the BS cell

3.1.2 Naming conventions

In the models, each reaction and metabolite is associated with a unique identifier. These identifiers are written according to a naming convention, in order to facilitate model manipulation and interpretation of simulation results. Metabolite IDs are organized according to the structure of **{Metabolite Name}_{Compartment}**. Three types of naming conventions are used for reaction IDs. Firstly, exchange reactions between the model and the extracellular space (uptake/secretion reactions) follow the convention **{Reaction Name}_tx**. Secondly, transport reactions between sub-cellular compartments have a **{Metabolite Name}_{Origin Compartment}{Destination Compartment}** structure. Finally, all other reactions follow a similar convention as with the metabolites with **{Reaction Name}_{Compartment}**. Metabolite and Reaction names are de-

rived from Metacyc ([136]) while the compartments are written as a one or two-letter abbreviation (Ex: Mitochondria - m; Plastid - p; Cytosol - c).

In the C_4 model, a prefix was added to each metabolite and reaction ID during the duplication process to identify the cell type. This results in the structure of **{[Cell Type]}_{Previous ID}**. Cell type prefixes can be either for the bundle sheath ([B]) or for the mesophyll ([M]). In addition, transport reactions of cytosolic metabolites between the cell types were named similarly to the exchange reactions but with an added prefix, with the structure of **{[MB]}_{Metabolite Name}_tx**.

3.1.3 Leaf architectural constraints

Added reactions

Missing transport reactions were added to the base model in order to enable a correct C_4 flux distribution. A malate/pyruvate shuttle was added to allow better export of pyruvate from the BS plastid during the C_4 cycle. A pyruvate/proton symporter was also added to improve pyruvate transport to the plastid (Table 1). Reactions were added according to the work of [17].

Table 1 – Transport reactions added to the base C_3 model to enable the C_4 cycle. Based on the model presented by [17].

Reaction Name	Reaction ID	Reaction Formula	Reference
Malate/Pyruvate transporter	PYR_MAL_pc	MAL_c + PYRUVATE_p ↔ MAL_p + PYRUVATE_c	[137]
Proton mediated Pyruvate symporter	PYR_H_pc	PROTON_c + PYRUVATE_c ↔ PROTON_p + PYRUVATE_p	[17]

Uptake reactions

The exchange of metabolites with the extracellular environment is performed either through uptake (source) or secretion (sink) reactions. In order to provide biologically interpretable flux solutions, the directionality of these reactions needed to be changed in some cases, while in others the exchange reaction needed to be outright blocked. Uptake of NH_4^+ was blocked in

order to prevent preferential uptake over NO_3^-. Only sucrose export was allowed in order to retain autotrophic growing conditions. Uptake of CO_2 from the medium was blocked in the BS, forcing the use of the C_4 metabolism to shuttle carbon from the M to the BS. This can be assumed due to reduced BS CO_2 leakiness under moderate temperature and incident irradiance [138] (Table 2). Uptake of CO_2 by the maize M cell was constrained to a maximum of 40 μmol m^{-2} s^{-1}, as reported in [139]. Additionally, the uptake of inorganic nutrients through the vascular bundle by the BS cells was simulated by blocking their uptake through the M cell, which now can only conduct gaseous exchanges (CO_2 and O_2) with the medium.

Table 2 – Constraints applied to the lower and upper bounds of the general and C_4 model. The value of 1000 μmol m^{-2} s^{-1} was defined as the maximum flux value. Constraining both lower and upper bounds results in a blocked reaction. Blocking the lower bound generates a source reaction while blocking the upper bound generates a sink reaction.

Reaction ID	Lower Bound	Upper Bound
Both Models		
H2O_tx	-1000	1000
NH4_tx	0	0
Nitrate_tx	0	1000
Pi_tx	0	1000
SO4_tx	0	1000
O2_tx	-1000	1000
Sucrose_tx	-1000	0
GLC_tx	-1000	0
Photon_tx	0	1000
unlProtHYPO_c	0	0
C_4		
[B]_CO2_tx	0	0
[M]_CO2_tx	0	40
[M]_Nitrate_tx	0	0
[M]_SO4_tx	0	0
[M]_H2O_tx	0	0
[M]_Ca_tx	0	0

Table 2 continued from previous page		
Reaction ID	**Lower Bound**	**Upper Bound**
[M]_Mg_tx	0	0
[M]_H2O_tx	0	0
[M]_Pi_tx	0	0
[M]_Ca_tx	0	0

Exchange reactions

Exchange of cytosolic metabolites was allowed between the M and BS in the C_4 model, with the exception of 47 metabolites which are presented in Table 3. This allows metabolites to be transported as needed between the cell types despite cell-type specific uptake from the medium. The list of metabolites whose transport was blocked is based on the work of [17].

Table 3 – List of cytosolic metabolites whose exchange is blocked between the bundle sheath and mesophyll cells in the C_4 model.

Metabolite Name	**Metabolite ID**	**Metabolite Name**	**Metabolite ID**
Hydrogen Sulfide (H_2S)	HS_c	Oxaloacetate ($C_4H_2O_5$)	OXALACETIC_ACID_c
Fructose 1,6-bisphosphate ($C_6H_{14}O_{12}P_2$)	FRUCTOSE_16_DIPHOSPHATE_c	Hydrogencarbonate (HCO_3)	HCO3_c
3-phospho-D-glyceroyl phosphate ($C_3H_4O_{10}P_2$)	DPG_c	UTP ($C_9H_{11}N_2O_{15}P_3$)	UTP_c
Proton (H^+)	PROTON_c	UDP ($C_9H_{11}N_2O_{12}P_2$)	UDP_c
Acetaldehyde (C_2H_4O)	ACETALD_c	UDP-α-D-glucose ($C_{15}H_{22}N_2O_{17}P_2$)	UDP_GLUCOSE_c

Table 3 continued from previous page			
Metabolite Name	**Metabolite ID**	**Metabolite Name**	**Metabolite ID**
Acetate ($C_2H_3O_2$)	ACET_c	ATP ($C_{10}H_{12}N_5O_{13}P_3$)	ATP_c
5,10-methenyl tetrahydrofolate ($C_{20}H_{22}N_7O_6$)	5_10_METHENYL_THF_c	ADP ($C_{10}H_{12}N_5O_{10}P_2$)	ADP_c
5-methyltetra hydrofolate ($C_{20}H_{25}N_7O_6$)	5_METHYL_THF_c	AMP ($C_{10}H_{12}N_5O_7P$)	AMP_c
L-homocysteine ($C_4H_9NO_2S$)	HOMO_CYS_c	IMP ($C_{10}H_{11}N_4O_8P$)	IMP_c
S-adenosyl-L-homo cysteine ($C_{14}H_{20}N_6O_5S$)	ADENOSYL_HOMO_CYS_c	XMP ($C_{10}H_{11}N_4O_9P$)	XANTHOSINE_5_PHOSPHATE_c
O-acetyl-L-serine ($C_5H_9NO_4$)	ACETYLSERINE_c	GTP ($C_{10}H_{12}N_5O_{14}P_3$)	GTP_c
Tetrahydrofolate ($C_{19}H_{23}N_7O_6$)	THF_c	GDP ($C_{10}H_{12}N_5O_{11}P_2$)	GDP_c
Adenosine ($C_{10}H_{13}N_5O_4$)	ADENOSINE_c	GMP ($C_{10}H_{12}N_5O_8P$)	GMP_c
Maltose ($C_{12}H_{22}O_{11}$)	MALTOSE_c	CDP ($C_9H_{12}N_3O_{11}P_2$)	CDP_c
coenzyme A ($C_{21}H_{32}N_7O_{16}P_3S$)	CO_A_c	dUMP ($C_9H_{11}N_2O_8P$)	DUMP_c
γ-L-glutamyl 5-phosphate ($C_5H_8NO_7P$)	L_GLUTAMATE_5_P_c	dTMP ($C_{10}H_{13}N_2O_8P$)	dTMP_c
Acetyl-CoA ($C_{23}H_{34}N_7O_{17}P_3S$)	ACETYL_COA_c	dTDP ($C_{10}H_{13}N_2O_{11}P_2$)	DTDP_c

Table 3 continued from previous page			
Metabolite Name	**Metabolite ID**	**Metabolite Name**	**Metabolite ID**
Cellulose ($(C_6H_{10}O_5)_n$)	CELLULOSE_c	GTP ($C_{10}H_{12}N_5O_{14}P_3$)	GTP_c
L-glutamate-5-semialdehyde ($C_5H_9NO_3$)	L_GLUTAMATE_GAMMA_SEMIALDEHYDE_c	dTTP ($C_{10}H_{13}N_2O_{14}P_3$)	DTTP_c
S-adenosyl-L-methionine ($C_{15}H_{23}N_6O_5S$)	S_ADENOSYL METHIONINE_c	NAD^+ ($C_{21}H_{26}N_7O_{14}P_2$)	NAD_c
Diphosphate ($H_4O_7P_2$)	PPI_c	NADH ($C_{21}H_{27}N_7O_{14}P_2$)	NADH_c
(S)-1-pyrroline-5-carboxylate ($C_5H_6NO_2$)	L_DELTA1_PYRROLINE_5_CARBOXYLATE_c	$NADP^+$ ($C_{21}H_{25}N_7O_{17}P_3$)	NADP_c
Ammonium (NH_4^+)	AMMONIUM_c	NADPH ($C_{21}H_{26}N_7O_{17}P_3$)	NADPH_c
Carbon dioxide (CO_2)	CARBON_DIOXIDE_c		

Rubisco

In C_3 plants, the M Rubisco oxygenase activity has been measured and is reported to have 3:1 carboxylase/oxygenase ratio [100]. In C_4, due to the carbon concentration mechanism, Rubisco oxygenase activity is negligible.

In the C_4 model, 3 Rubisco populations were implemented. One population was implemented in the M cell and was constrained to a 3:1 carboxylation/oxygenation ratio. Another was implemented in the BS cell, uses the CO_2 transported through the C_4 cycle and was subjected to no carboxylation/oxygenation ratio. The last was implemented in the BS and was

constrained to only use CO_2 directly imported from the M cell and was also constrained to a 3:1 carboxylation/oxygenation ratio [17]. The purpose of this last population was to observe the model choice between the cost of the C_4 cycle and photorespiration.

3.1.4 VOLUMETRIC CONSTRAINTS

In our modeling approach, two interacting systems, corresponding to the BS and M tissue are being modeled. These two systems are spatially separated and light uptake into the systems is modelled independently and is regulated by the ratio between light uptake by the BS cell and light uptake by the M cell ($AB_{\frac{BS}{M}}$, no unit). Observation of figure 2, however shows that, not only are the BS cells surrounded by M cells, when looking at a section of leaf surface, there are areas that are exclusively occupied by M tissue and areas occupied by BS tissue. As such, only the $AB_{\frac{BS}{M}}$ is not sufficient to accurate model the light uptake by each system. By accounting for these different tissue surface areas through a the implementation of a volume ratio constraint ($V_{\frac{BS}{M}}$, no unit), we can describe this effect.

Anatomical constraints were implemented into our constraint-based modelling framework through a volume ratio constraint between the BS and the M tissue ($V_{\frac{BS}{M}}$). Leaf thickness ($V_{Thickness}$, m) was equal for both cell and therefore $V_{\frac{BS}{M}}$ was calculated as the ratio between the BS (V_{BS}, m^2) and M (V_M, m^2) tissue surface area as described in equation 5.

$$
\begin{aligned}
V_{BS} &= (V_{Width})^2 \cdot V_{Thickness} \\
V_M &= (IVD - V_{Width})^2 \cdot V_{Thickness} \\
V_{\frac{BS}{M}} &= \frac{V_{BS}}{V_M} \\
V_{\frac{BS}{M}} &= \frac{(V_{Width})^2 \cdot V_{Thickness}}{(IVD - V_{Width})^2 \cdot V_{Thickness}} \\
V_{\frac{BS}{M}} &= \frac{(V_{Width})^2}{(IVD - V_{Width})^2}
\end{aligned}
\tag{5}
$$

BS surface area was approximated by squaring leaf vasculature width (V_{Width}, m), while M surface area was approximated by squaring the difference between the interveinal distance (IVD, m) and V_{Width}. Data was collected for maize leaf anatomical measurements from [131].

Exchange stoichiometry

The calculated $V_{\frac{BS}{M}}$ ratio was then used to constrain the stoichiometry of the exchange reactions between the M and the BS cell. Model flux units are given in μmol as a function of area (m^2) and time (s). Because of this relationship, moving flux from one compartment to another compartment with a larger or smaller area leads to a downscale or upscale in flux, respectively, once the flux unit is scaled. To compare the flux values between the cell types, fluxes are multiplied by the volume value of their respective cell type and have their units converted to μmol s^{-1}. This is illustrated in Figure 13, given an example where $V_{\frac{BS}{M}} = 4$.

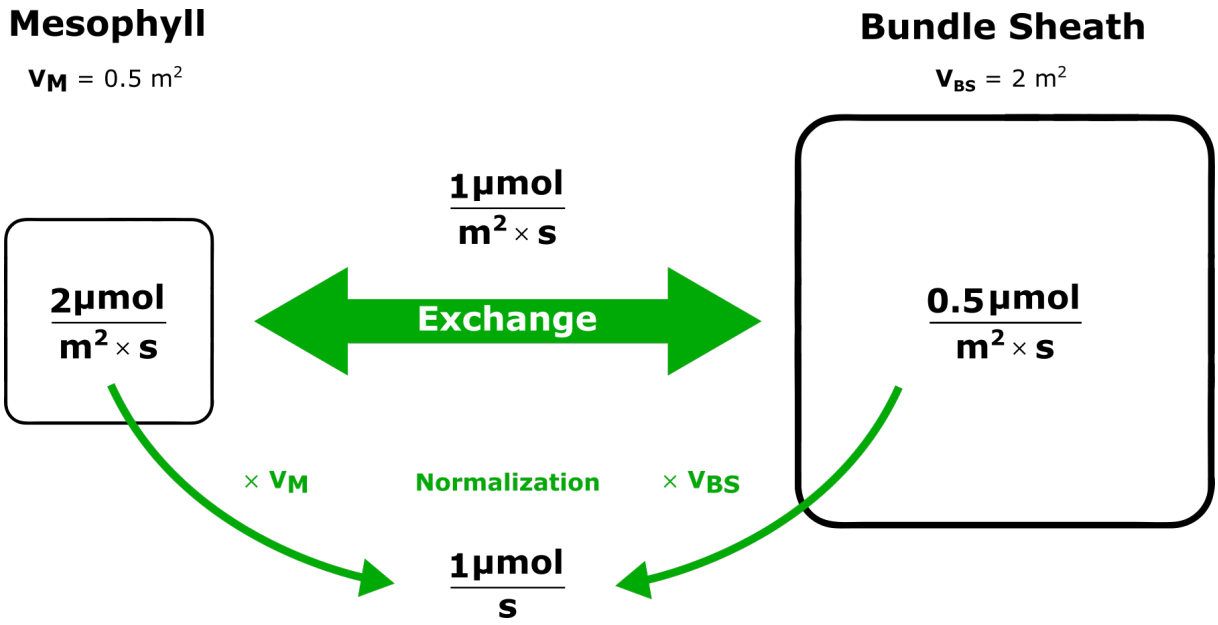

Figure 13 – Representation of the flux scaling through the exchange reactions between the M and BS cell with the implementation of surface area differences. The green arrows represent the exchange reaction and the scaling process. It must be noted that although V_M and V_{BS} are referred to as volumes, their unit is in m^2, as described in equation 5.

In this way, if V_M is assumed to always have an area of 1 m^2, all metabolite exchange reactions between the M and BS cells had their stoichiometries scaled in such a way that $1\ \frac{\mu mol}{m^2\ s}\ [M]\_Metabolite\_c \leftrightarrow 1/V_{\frac{BS}{M}}\ \frac{\mu mol}{m^2\ s}\ [B]\_Metabolite\_c$. This results in a simulation of the effect of relative tissue sizes upon metabolite transport between the cell types.

Light uptake

Light uptake into the model was defined separatly as the light uptake into the BS (P_{BS}, μmol m^{-2} s^{-1}) and light uptake into the M cell (P_M, μmol m^{-2} s^{-1}). To compare light uptakes with bibliographically reported values, P_{BS} and P_M were normalized by multiplying them by the respective areas of their cells, like described in figure 13. These values were then summed, originating P_{Total} (μmol s^{-1}) (Equation 6).

$$P_{Total} = P_{BS} \cdot V_{BS} + P_M \cdot V_M \tag{6}$$

The M cells surround their neighbouring BS cells, leading to a shading effect, in which the BS cells receive less light than the M cells [140]. To model this effect, normalized P_{BS} and P_M values are allocated through the introduced through the ($AB_{\frac{BS}{M}}$) ratio (Equation 7), which was implemented in previous works [17]. When $AB_{\frac{BS}{M}} = 1$ and $V_{\frac{BS}{M}} = 1$, $P_BS = P_M$.

$$AB_{\frac{BS}{M}} = \frac{P_{BS} \cdot V_{BS}}{P_M \cdot V_M} \tag{7}$$

From the values of V_{BS}, P_{Total} and $AB_{\frac{BS}{M}}$ the values of P_M and P_{BS} need to be calculated in order to be supplied to the model as constraints for the photon uptake reaction of the respective cell types. We first deduced the formula for the calculus of P_{BS} from Equation 6 (Equation 8) and from Equation 7 (Equation 9).

$$P_{BS} = \frac{(P_{Total} - P_M \cdot V_M)}{V_{BS}} \tag{8}$$

$$P_{BS} = AB_{\frac{BS}{M}} \cdot P_M \cdot \frac{V_M}{V_{BS}} \tag{9}$$

In the same way, Equation 6 and Equation 9 were combined to deduce the formula for the calculus of P_M. This resulted in Equation 10, which calculates P_M from the known values of P_{Total}, V_M and $AB_{\frac{BS}{M}}$.

$$
\begin{aligned}
P_{Total} &= \left(AB_{\frac{BS}{M}} \cdot P_M \cdot \frac{V_M}{V_{BS}} \right) \cdot V_{BS} + P_M \cdot V_M \\
&= AB_{\frac{BS}{M}} \cdot P_M \cdot V_M + P_M \cdot V_M \\
&= \left(AB_{\frac{BS}{M}} + 1 \right) \cdot P_M \cdot V_M
\end{aligned}
$$

By rearranging the equation, we obtain:

$$
P_M = \frac{P_{Total}}{\left(AB_{\frac{BS}{M}} + 1 \right) \cdot V_M} \tag{10}
$$

As previously mentioned, if V_M is normalized to always take the value of 1 m^2 ($V_M = 1$), then $V_{\frac{BS}{M}} = V_{BS}$. This allows the simplification of equations 10 and 8, resulting in equation 11 and 12, respectively, which are implemented into the model.

$$
P_M = \frac{P_{Total}}{\left(AB_{\frac{BS}{M}} + 1 \right)} \tag{11}
$$

$$
P_{BS} = \frac{(P_{Total} - P_M)}{V_{\frac{BS}{M}}} \tag{12}
$$

3.1.5 Internal constraints

General constraints

Plastoquinol Oxidase, NTT, and uncoupled pyruvate transport were blocked according to [17]. Unutilized biomass reactions already present in the model were blocked in order to prevent unwanted sink reactions. ATP maintenance cost reaction acts exclusively as an ATP sink, and its directionality was constrained to only allow ATP consumption. PPDK is located mostly in M cells in the plastid compartment [33]; transport of pyruvate was achieved by blocking this reaction in the cytosol in the M cell.

In maize, FNR is membrane-bound in the BS, mostly capable of $NADP^+$ photoreduction, while it is present in both membrane-bound and soluble form in the M, being capable of both

$NADP^+$ photoreduction and reducing ferredoxin. Constraints for FNR in the model were updated to reflect this, with unconstrained directionality assigned to FNR in the M cell, and only allowed in the direction of $NADP^+$ photoreduction in the BS cell. PSII is lacking in the BS of Maize and was therefore blocked. All added internal constraints are detailed in Table 4.

Table 4 – List of constraints used in the model curation of internal reactions in the C_3 and C_4 models.

Reaction ID	Lower bound	Upper bound	Reference
Both Models			
Plastoquinol_Oxidase_p	0	0	[141]
ATP_ADP_Pi_pc	0	0	[142]
PYRUVATE_pc	0	0	[17]
Biomass_tx	0	0	
AraCore_biomass_tx	0	0	-
ATPase_tx	0	1000	
C_4			
[M]_PYRUVATEORTHOPHOSPHATE_DIKINASE_RXN_c	0	0	[33]
[B]_PSII_RXN_p			[143]
[M]_1_PERIOD_18_PERIOD_1_PERIOD_2_RXN_p	1000	1000	[144]
[B]_1_PERIOD_18_PERIOD_1_PERIOD_2_RXN_p	0	1000	

Carbon concentrating mechanism

Analysis of initial FBA solutions revealed no C_4 cycle activity. Traceback of C metabolism revealed that the C_4 cycle was bypassed through the reverse usage of TCA cycle and urea degradation reactions. This was corrected by manipulating the directionality of the involved reactions to allow decarboxylation through the C_4 pathway (Table 5).

Table 5 – List of constraints applied in order to regulate alternative decarboxylation pathways and enable the C_4 cycle.

Reaction ID	Lower bound	Upper bound
[B]_UREASE_RXN_c	0	0
[M]_UREASE_RXN_c	0	1000
[B]_CARBAMATE_KINASE_RXN_p	0	1000
[M]_CARBAMATE_KINASE_RXN_p	0	1000
[B]_ISOCITDEH_RXN_m	0	1000
[M]_ISOCITDEH_RXN_m	0	1000
[B]_ISOCITDEH_RXN_c	0	1000
[M]_ISOCITDEH_RXN_c	0	1000
[B]_ISOCITRATE_DEHYDROGENASE_NAD_RXN_m	0	1000
[M]_ISOCITRATE_DEHYDROGENASE_NAD_RXN_m	0	1000

Light-dependent maintenance

Light-dependent maintenance was implemented as described in [35]. It results in the implementation of equation 13, in which x represents a photon uptake and y represents maintenance ATPase reaction flux, which is an ATP sink reaction. Such an implementation was designed to include the costs of non-growth associated cellular maintenance into the model and is present in each cell-type in the C_4 model.

$$\mathrm{y} = 0.0049\mathrm{x} + 2.7852 \tag{13}$$

Additionally, a previous study reported values for ATP and NADPH consumption in *Arabidopsis thaliana* heterotrophic cell cultures under control conditions [145]. This data was implemented into the model by constraining NADPase reactions (NADPH sink reaction) to have a combined one unit of flux for every three units of flux through the ATPase reaction (3:1 ATPase/NADPase), whose value is determined by the light uptake according to Equation 13. There are three NADPase reactions in each cell, in the plastid, mitochondria and cytosol compartments, and the model freely chooses which should carry flux.

3.2 FLUX SIMULATIONS

For the model simulations, pFBA was used. The solver used to run the linear optimisations was ”Gurobi”.

3.2.1 SVG FLUX MAPS

Flux solutions were visualised by integrating pre-made graphs of metabolic pathways with flux data from model simulations. The program Inkscape [146] was used to manually generate SVG flux metabolic maps. Flux solutions were saved as Pandas dataframes and then reaction flux data was mapped to the corresponding arrows in the SVG map. Mapped flux data was then scaled and implemented into the arrows both as a colour gradient and as arrow width.

3.2.2 BUDGET PLOTS

Metabolite turnover was analysed through a pair of stacked barplots in which one bar contains flux values of metabolite-consuming reactions, while the other contains flux values of metabolite-producing reactions. In every reaction, the budgeted metabolite stoichiometry was multiplied by the reaction flux value as a scaling procedure.

4

RESULTS AND DISCUSSION

4.1 LEAF BIOMASS COMPOSITION

A biomass reaction was built for maize, considering a set of 28 metabolites, representing carbohydrate, protein, cell wall, lipid and soluble metabolite components. This biomass reaction represents a sink reaction in which the relative percentages of the components needed for cellular growth are represented as stoichiometries of each metabolite, which, when summed, lead to one flux unit of biomass. The leaf-specific stoichiometries were derived mostly from [102], with starch, maltose, glucose, sucrose and fructose drawn from [101] and cellulose from [135] models biomass equations. Before adding the reaction to the model, the stoichiometric coefficients for each metabolite were converted to the same units (mM) and scaled to 100. Scaling was performed to allow the interpretation of the biomass reaction flux value as the result of the relative contribution of each of its components. The scaled stoichiometries were then used to create the maize biomass equation and added to the models (Fig. 14).

Analysis of the used biomass composition shows that the biggest contributor to the biomass corresponds to carbohydrates, with approximately 53% contribution to total biomass, followed by proteins (39%), cell wall (3.69 %), lipids (3.6%) and soluble metabolites (0.8 %). This is consistent with previously measured compositions of maize leaves, which identified C as the most abundant nutrient in maize leaves both in control and elevated temperature conditions [147].

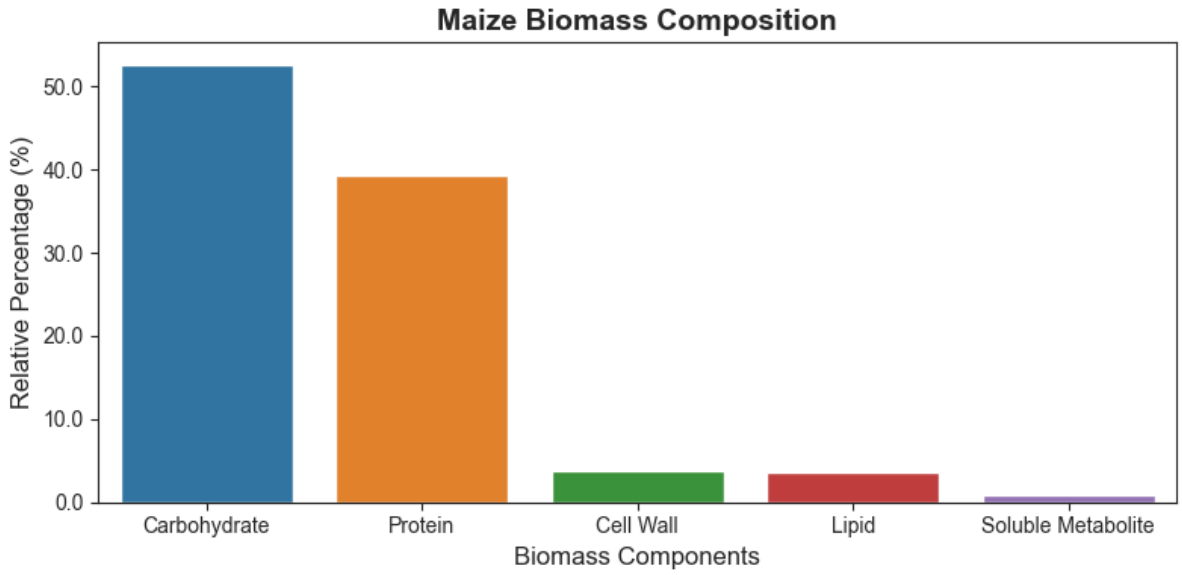

Figure 14 – Representation of the relative percentages of each class of metabolites contribution to the Maize biomass equation.

4.2 Maize C_4 model

The maize C_4 model results from the duplication of a generic model capable of C_3 photosynthesis. This results in a total of 1722 metabolites and 1792 reactions. The initial version of the generic C_3 model corresponded to the ”Core” version. This model version was obtained through the deprotonation of the original ”ProtonationStateCore” model. The advantages of the ”Core” version lay in the absence of calculation of the protonation and subsequent reaction stoichiometry changes whenever reactions needed to be added to the model. Protonation data is difficult to obtain and implement into the model. Issues within the ”Core” version required additional curation, leading to the ”ProtonStateCore” version being used in this work.

4.2.1 Prediction of C_4 cycle

Maize primarily uses the C_4 photosynthetic pathway of NADP-ME, with a smaller engagement of the PEP-CK pathway. After initial fixation of C into OAA by PEPC, the C_4 molecule is then either converted to aspartate in the cytosol by the reversible action of aspartate aminotransferase (AspAT) or into malate in the plastid by the action of malate dehydrogenase. These molecules

are then transported to the BS directly through the plasmodesmata. In the case of aspartate, it is converted back into OAA by AspAT and then decarboxylated into PEP by PEP-CK, which is transported back to the M cell to serve again as a substrate to PEPC. On the other hand, malate is transported to the plastid where it is decarboxylated by NADP-ME yielding pyruvate. This pyruvate is transported back into the M cell plastid where it is converted to PEP by PPDK, which is transported to the cytosol to also serve as a substrate to PEPC. Maize is known to operate both of these C_4 cycle subtypes simultaneously.

The C_4 model was able to accurately simulate each of these subtypes individually and also simulate their co-activity (Figure 15)). This was only possible after the application of the curation described in chapter 3. After blocking or constraining to high photorespiratory flux the M cell Rubisco, and blocking direct CO_2 transport between the cell types, the model predicted biologically unfeasible decarboxylation routes through urea metabolism and through the partially reversed activity of the TCA cycle. The root of this issue was identified as the lack of alternative transportation routes of malate into the BS cell plastid and pyruvate into the M cell plastid. Malate transport was solved by adding a Mal/Pyr shuttle, while pyruvate transport implied blocking PPDK in the M cell cytosol and adding a Pyruvate/H^+ symporter into the M cell plastid.

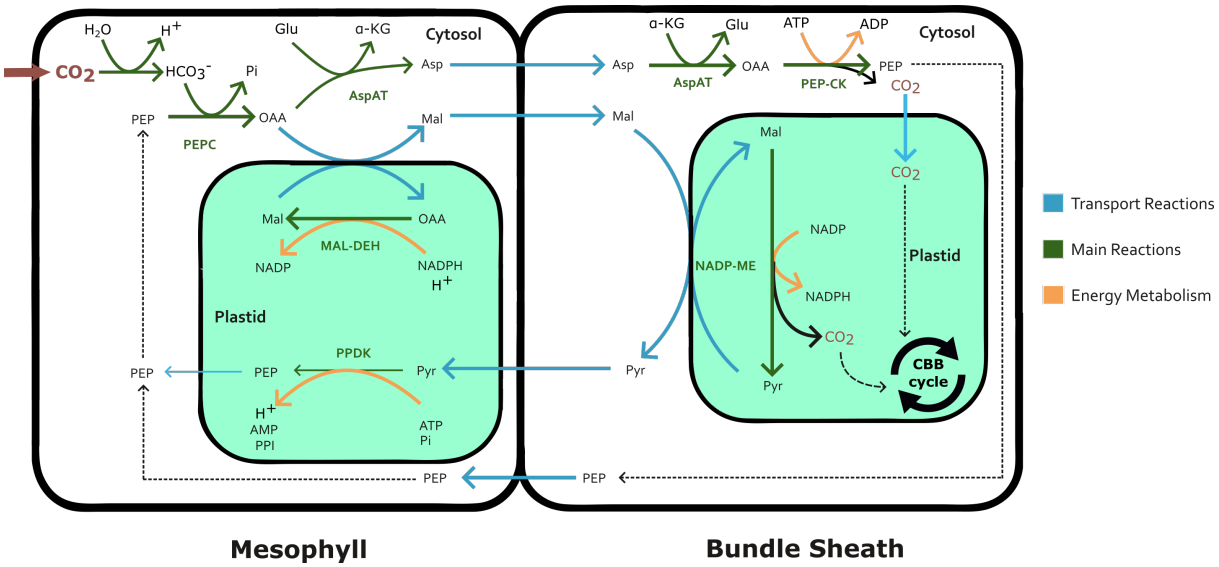

Figure 15 – FluxMap representing NADP-ME/PEP-CK C_4 photosynthetic metabolism as represented in the C_4 model. The main reactions are represented in dark green, associated energy metabolism is represented in yellow and transport reactions are represented in light blue. Abbreviations: HCO_3- - Bicarbonate; Pi - phosphate; OAA - Oxaloacetate; Glu - glutamate; α-KG - α-ketoglutarate; Asp - Aspartate; Mal - Malate; MAL-DEH - Malate dehydrogenase; Pyr - pyruvate; PEP - phosphoenolpyruvate.

4.2.2 Implementation of anatomical constrains improves prediction of C_2 photosynthesis under photorespiratory conditions

To validate the introduced anatomical constraints in the maize C_4 model, we designed an experiment to test their impact on GDC activity in the M and BS mitochondria. The glycine pump was previously introduced in chapter 2.1.2. To enable photorespiratory activity in the C_4 model, the BS Rubisco using CO_2 from the C_4 cycle was constrained to a 10:1 carboxylation/oxygenation ratio, while the M Rubisco was kept at 3:1 carboxylation/oxygenation ratio. The BS Rubisco which used CO_2 directly imported from the M cell was blocked. A high photorespiratory environment was also simulated by enforcing a high light uptake (P_{Total}) of 1000 μmol s^{-1}. Additionally $AB_{\frac{BS}{M}}$ value was also set at 0.66. We then tested GDC activity under two volume constrain scenarios using FVA (Figure 6). In one scenario, the cell was assumed to have equal volume i.e the $V_{\frac{BS}{M}}$ was set to a value of 1, while in the other $V_{\frac{BS}{M}}$ was set at 5.3 like previously calculated. FVA was run with the additional constraint that the total sum of absolute fluxes could not be larger than the smallest possible sum of absolute fluxes i.e that the total sum of absolute fluxes could not be larger than the pFBA solution.

Table 6 – Maximum and minimum flux values of GDC enzyme in the BS and M cells under two volumetric constraints.

Flux / Volume	M GDC		BS GDC	
	Max	Min	Max	Min
$V_{\frac{BS}{M}} = 1$	1.859	1.859	5.936	5.936
$V_{\frac{BS}{M}} = 5.3$	0	0	7.651	7.651

In the absence of volume constraints, we observe that GDC activity is detected in both the M and BS cells, although BS GDC still presents a much higher GDC activity. The higher BS GDC activity can perhaps be explained by the large light uptake by the BS cell thanks to the $AB_{\frac{BS}{M}}$ of 0.66 enabling more energy production for operating the glycine pump. The reported

$AB_{\frac{BS}{M}}$ is considered a high value associated with a C_4 phenotype, while C_3 plants normally display lower $AB_{\frac{BS}{M}}$ values. When the volume constraint is implemented, a full shift of the GDC pump occurs to the BS cell, with no M GDC activity.

It should be noted that both of these scenarios correspond to flux solutions in which most of the Rubisco activity occurs in the M cell, despite the high photorespiratory ratio. This occurs because the very high light uptakes lead to an abundance of energy production in both cell types, which makes the cost of a higher photorespiratory activity less relevant and therefore a better flux solution for the imposed constraints than the usage (and cost) associated with operating the C_4 cycle. When M Rubisco activity is allowed, BS Rubisco and the C_4 cycle become more preferential under more moderate (500 μmol s^{-1}) light uptakes. Despite this seemingly disagreeing with the conditions for C_4 evolution (high light intensities), it must be stated that the model lacks temperature-regulated Rubisco oxygenase activity, and therefore the impact of photorespiration on the M cell is underestimated in the C_4 model under high light intensities.

Overall, the implementation of the volume ratio constraint predicts a fully operational C_2 photosynthesis flux mode with GDC activity exclusively in the BS cell. Compared to the bibliography, this represents an improvement when we look at the absence of a volume ratio constraint implementation scenario.

4.2.3 Triose phosphate-3-phosphoglycerate shuttle predicted with an anatomy-constrained C_4 model

In C_4 metabolism, the M cell harvests more light than the BS cell, producing ATP and NADPH through linear electron transport. However, the BS cell operates the CBB cycle, which increases its demand for NADPH and ATP. To provide the BS cell with these metabolites during C_4 photosynthesis, the triose phosphate-3-phosphoglycerate shuttle emerges. In this shuttle, 3-phospho-D-glycerate (G3P) is sent through the plasmodesmata to the M cell plastid where it is phosphorylated at the expense of ATP by phosphoglycerate kinase into 3-phospho-D-glyceroyl phosphate (DPG). DPG is then reduced by the action of glyceraldehyde-3-phosphate dehydrogenase into D-glyceraldehyde 3-phosphate (GAP) at the expense of NADPH and a H^+.

GAP is then transported back to the BS cell where the formerly mentioned reactions operate in reverse, originating ATP, NADPH and H^+ for use by BS cell metabolism.

We tested the operation of the shuttle in the C_4 model in the presence and absence of volume constraints (Figure 16). For model simulations parameters P_{Total} was set at 700 μmol s^{-1}, $AB_{\frac{BS}{M}}$ was set at 0.66 and the M and photorespiratory BS Rubisco were blocked.

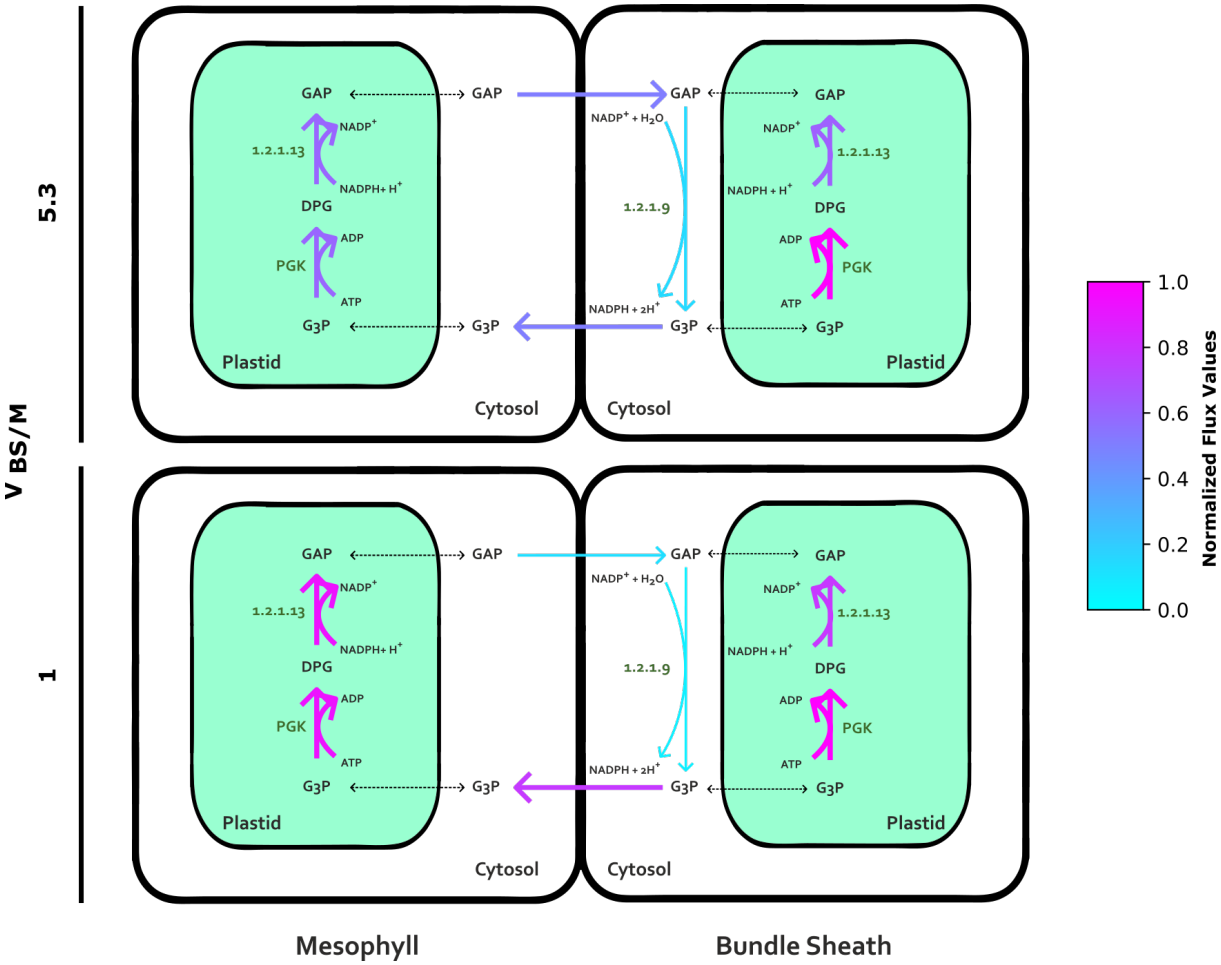

Figure 16 – FluxMaps of the triose phosphate-3-phosphoglycerate shuttle with integrated flux data under two volume constraint scenarios. Flux data is shown through the colour gradient and arrow width. Some reactions are represented by their EC numbers. Abbreviations: GAP - D-glyceraldehyde; G3P - 3-phospho-D-glycerate; DPG - 3-phospho-D-glyceroyl phosphate;PGK - phosphoglycerate kinase; 1.2.1.13 - glyceraldehyde-3-phosphate dehydrogenase (NADP+) (phosphorylating); 1.2.1.9 - glyceraldehyde-3-phosphate dehydrogenase (NADP+).

Flux solutions were visualized by drawing an SVG flux map and integrating the flux values of the corresponding reactions. When the volume ratio was not enforced, the shuttle was only partially active, with G3P being produced in the BS by the activity of Rubisco and then shuttled back to the M cell, with no GAP being shuttled back. With the implementation of the $V_{\frac{BS}{M}}$ of 5.3,

we observe a functional complete shuttle between the cell types, with G3P being sent to the M plastid and GAP being sent back to the BS cytosol. Interestingly, the release of reducing power stored in GAP does not occur in the plastid but directly in the cytosol under the activity of glyceraldehyde 3-phosphate dehydrogenase, which directly converts GAP into G3P releasing NADPH and 2 H^+, while plastidial reactions still convert G3P into DPG and GAP. This means that the production of GAP in the BS is still vital to an optimum flux solution in the BS cell and the cytosolic reaction is utilized as a means of harvesting the energy from the shuttle.

4.3 Impact on anatomical constraints on nitrate metabolism

4.3.1 Anatomy-constrained C_4 model predicts glutamate dehydrogenase activity during nitrogen assimilation

Besides energy metabolism, N assimilation was also investigated in the presence and absence of volume constraints. To investigate this, 2 flux simulations were performed and the flux solutions were obtained. One was performed without the implementation of the volume constraint, i.e $V_{\frac{BS}{M}} = 1$; another was performed with the implementation of previously calculate $V_{\frac{BS}{M}} = 5.3$, representing the value for maize. Flux simulation were ran with $P_{Total} = 700$ μmol s^{-1} and $AB_{\frac{BS}{M}} = 0.66$. M and BS photorespiratory Rubisco were blocked to ensure C_4 cycle exclusive activity. The resulting flux values were integrated with pre-designed SVG flux maps of C_4 N assimilatory metabolism (Figure 17).

Analysis of the flux maps shows that, in both scenarios, initial NO_3^- assimilation occurs in the M cell. This is according to the distribution of C_4 N assimilation reported in [73]. Additionally, GS-GOGAT activity is located in the M cell, whereas the same author reports GS-GOGAT activity in both the BS andM cell or exclusively in the BS cell.

Interestingly, while in the $V_{\frac{BS}{M}} = 1$ scenario GS-GOGAT fluxes are fully explained by NO_3^- uptake, in the $V_{\frac{BS}{M}} = 1$ scenario the greatest contribution for GS-GOGAT comes from NH_4^+ originating from the BS cell resulting from the activity of Glutamate Dehydrogenase (GDH). The enzyme GDH is involved in C and N metabolism and was initially thought to act as an alternative pathway for ammonium assimilation. However, later in vivo studies revealed that the enzyme

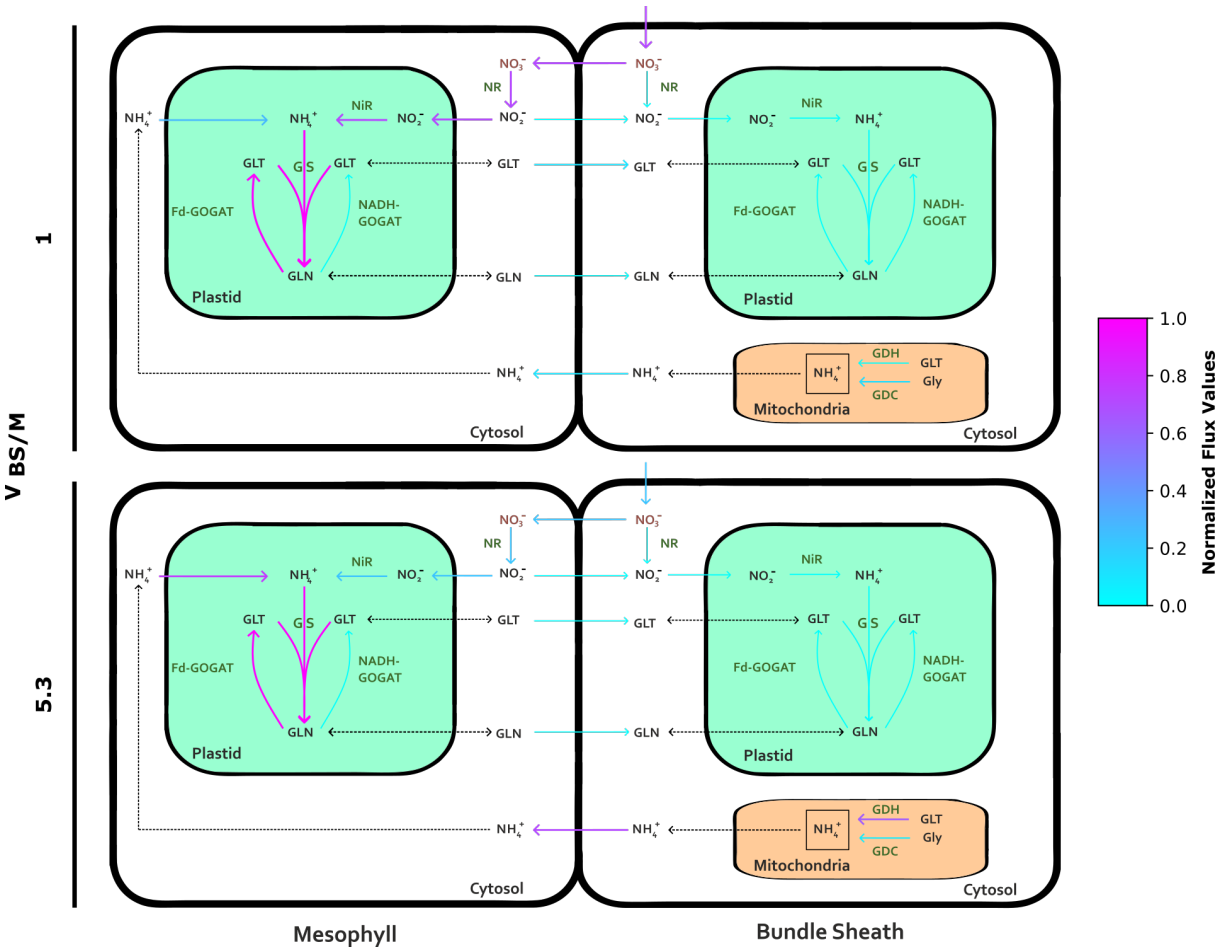

Figure 17 – FluxMaps of the nitrogen assimilation metabolism with integrated flux data under two volume constraint scenarios. Flux data is shown through the colour gradient and arrow width. Abbreviations: NR - Nitrate reductase; NiR - Nitrite reductase; GS - Glutamine synthase; GOGAT - Glutamate synthase; GDH - Glutamate dehydrogenase; GDC - Glycine decarboxylase; GLT - Glutamate; Gly - Glycine; GLN - Glutamine.

operated in the direction of glutamate deamination. Further studies in maize localized this enzyme exclusively to the BS cell. The physiological function and the reason why it operates in the direction of deamination are not understood [148]. In our analysis, we observe that GDH is activated when $V_{\frac{BS}{M}}$ is implemented and provides NH_4^+ for assimilation by GS-GOGAT. Besides providing NH_4^+ from glutamate, this enzyme also provides carbon skeletons to the BS through the production of α-ketoglutarate which can be used for additional cellular activities.

4.3.2 Improvement of mesophyll-specific nitrate reduction prediction under a range of light uptakes with the application of anatomical constraints

After observing N metabolism in two specific light uptake scenarios, we wanted to verify how the implementation of $V_{\frac{BS}{M}}$ affected N metabolism across a wider range of parameters, particularly with regards to initial NO_3^- assimilation. We defined a wide grid of $AB_{\frac{BS}{M}}$ and P_{Total} values and performed flux simulations for every parameter combination. This was performed with $V_{\frac{BS}{M}}$ set at 1 and 5.3. For each simulation, the cellular location of NiR was determined and qualitatively mapped. The results were used to build two heatmaps (Figure 18).

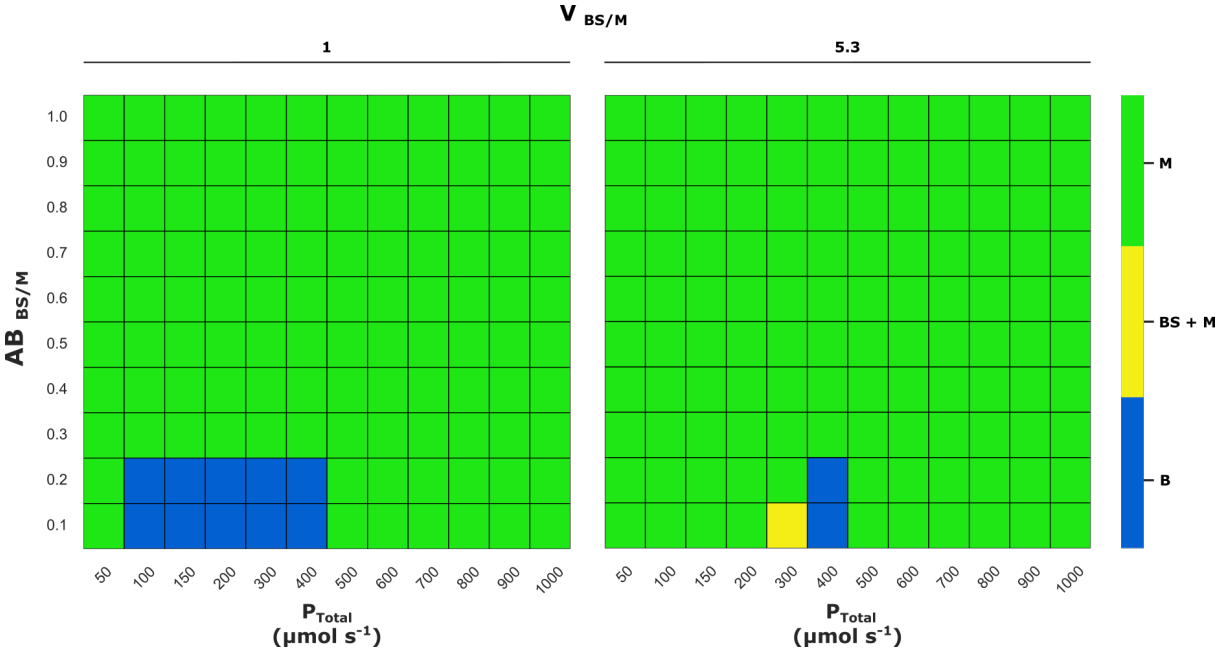

Figure 18 – Qualitative heatmaps of the cellular localization of nitrate reduction in the C_4 model for a range of light uptakes and light distributions. Green, blue and yellow squares represent mesophyll-located, bundle sheath-located and mixed flux solutions, respectively.

The resulting data shows that, when $P_{Total} < 500\,\mu mol\,s^{-1}$ and $AB_{\frac{BS}{M}} < 0.3$, BS located NiR is preferred when no volume constraint is applied. With the volume constraint, BS assimilation only occurs for $P_{Total} = 400\,\mu mol\,s^{-1}$ for $AB_{\frac{BS}{M}} < 0.3$, while joint BS and M NiR activity are predicted when $P_{Total} = 300\,\mu mol\,s^{-1}$ for $AB_{\frac{BS}{M}} = 0.1$.

Overall, these results indicate that there is an improvement in the prediction of NiR activity across the spectrum of light uptake scenarios when compared to the biologically reported metabolic distributions of C_4 N assimilation through the implementation of the volume constraint.

4.4 Changes in decarboxylation enzymes activity predicted under a range of volume ratios and light uptakes

Maize utilizes two subtypes of C_4 photosynthesis in tandem, PEP-CK and NADP-ME. The two subtypes differ in their energetic requirements and the sub-cellular division in which they operate. We investigated how variation in $V_{\frac{BS}{M}}$ affects the choice of decarboxylation enzyme in the C_4 model. Three P_{Total} uptake scenarios were selected, corresponding to low (250 μmol s^{-1}), medium (500 μmol s^{-1}) and high (750 μmol s^{-1}) light uptakes. Additionally, M and photorespiratory BS Rubisco were blocked to ensure activity of the C_4 cycle. For each of these scenarios, flux solutions were obtained using pFBA for a range of $V_{\frac{BS}{M}}$ and $AB_{\frac{BS}{M}}$ values. These flux solutions were then used to plot two heatmaps per scenario: one for PEP-CK and another for NADP-ME. The value computed for each flux solution corresponds to the ratio of decarboxylation with CO_2 uptake for each of the decarboxylation enzymes (Figure 19).

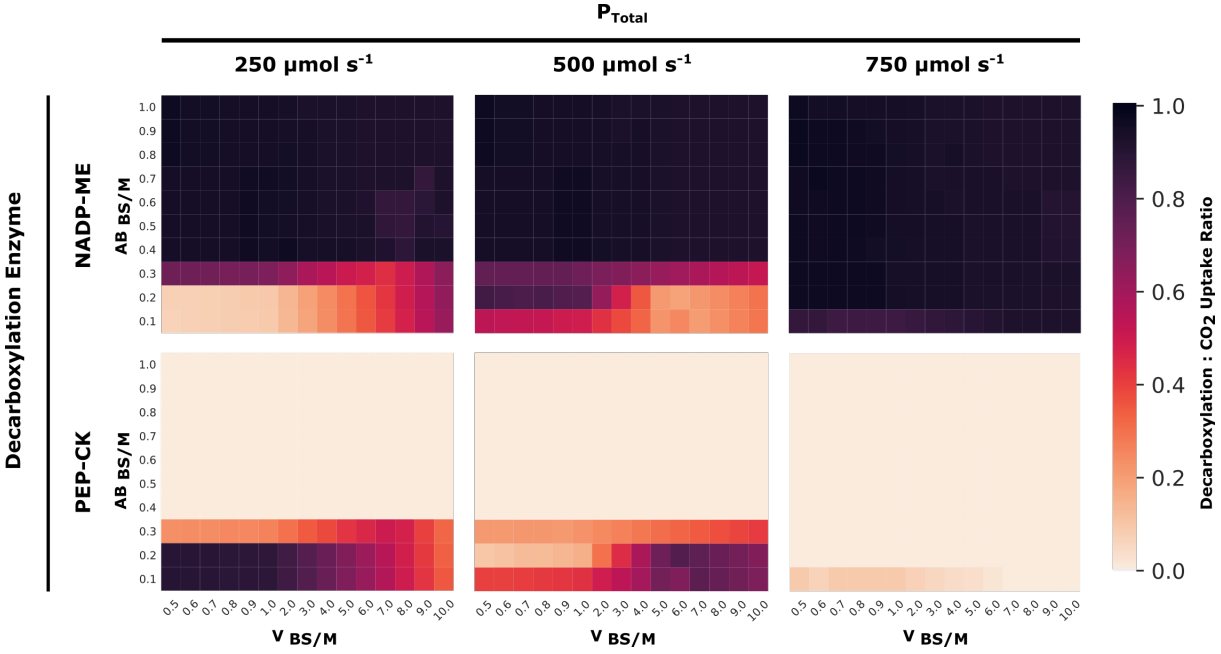

Figure 19 – Heatmaps for NADP-ME and PEP-CK activity in the BS cell. For each total photon uptake scenario, the ratio between enzymatic decarboxylation and CO_2 uptake is calculated for each enzyme for a range of volume constraints and light distributions. These ratios are then plotted separately for each enzyme. The sum of the ratio values for each light uptake scenario is equal to 1.

Firstly, under high light uptakes, NADP-ME is exclusively utilized for decarboxylation, regardless of $V_{\frac{BS}{M}}$ and $AB_{\frac{BS}{M}}$ value, with activity of PEP-CK only present in very small amounts under a $AB_{\frac{BS}{M}}$ value of 0.1, which represents a very low light uptake by the BS cell.

Secondly, under medium light uptakes, NADP-ME is the dominant decarboxylation enzyme when $AB_{\frac{BS}{M}} > 0.3$. When $AB_{\frac{BS}{M}} = 0.3$, a gradient of co-activity between NADP-ME and PEP-CK occurs along the $V_{\frac{BS}{M}}$ axis, with smaller $V_{\frac{BS}{M}}$ values associated with higher NADP-ME activity, which give way to PEP-CK activity as the $V_{\frac{BS}{M}}$ increases. When $AB_{\frac{BS}{M}} \leq 0.2$ flux solutions with higher $V_{\frac{BS}{M}}$ values continue to exhibit higher PEP-CK activity, which becomes dominant around $V_{\frac{BS}{M}} = 3$, while lower $V_{\frac{BS}{M}}$ values exhibit NADP-ME high activity ($AB_{\frac{BS}{M}} = 0.2$) or, curiously, a fixed value for PEP-CK activity ($AB_{\frac{BS}{M}} = 0.1$).

Finally, under low light uptakes, this scenario is very similar to the medium light uptake scenario while $AB_{\frac{BS}{M}} > 0.3$. Looking at $AB_{\frac{BS}{M}} \leq 0.3$, lower $V_{\frac{BS}{M}}$ values lead to the display of predominant PEP-CK activity which gradually engages with co-activity with NADP-ME at higher $V_{\frac{BS}{M}}$.

Previous studies, both in vivo and in silico, have confirmed NADP-ME as a preferential decarboxylation enzyme in a scenario where light is not limiting [17], while PEP-CK is typically more engaged in light limiting scenarios, particularly with lower light uptake by the BS. In our model light becomes not limiting when CO_2 uptake becomes limiting. i.e the maximum of uptake of 40 μmol m^{-2} s^{-1} of CO_2 is being met. Our modelling approach shows that PEP-CK engagement occurs predominantly under lower light uptakes by the BS under light limitation. This is further evidenced by higher PEP-CK activity under low light scenarios in lower $V_{\frac{BS}{M}}$ values. Observing the biochemistry of the BS cell of Maize, the lack of PSII leads to its specialization in cyclic electron transport. Usage of PEP-CK increases the need for cytosolic ATP in the BS cell. Therefore, it is possible that PEP-CK engagement in these conditions is prefered by pFBA to take advantage of elevated BS ATP production ratio when compared to the M cell, and therefore maximize CO_2 fixation under sub-optimal conditions while balancing energetic requirements. Higher $V_{\frac{BS}{M}}$ imply more light uptake by the BS, which may disable this flux mode and shift decarboxylation towards NADP-ME activity. It should be noted however, that many C_4 species display higher $AB_{\frac{BS}{M}}$ including maize which our simulations predict as exclusively NADP-ME, while in vivo maize displays a NADP-ME/PEP-CK co-activity phenotype. This may

imply that the demand for reducing power in the M cell in the form of NADPH may be under represented in our model.

4.5 Cyclic eletron transport predicted in bundle sheath cells under low light conditions

In maize, BS cells are specialized in ATP production through the exclusive usage of cyclic electron transport in the plastid. The activity of PEP-CK increases BS demand for ATP, and our simulations predict it to be prevalent in low light conditions and lower $V_{\frac{BS}{M}}$ values. These observations led us to further attempt to validate the link between BS ATP production, light uptake and anatomical constraints, while also testing the C_4 models' ability to generalize and provide broader interpretations of the observed flux distributions.

We tested this by first sourcing data from [61]. In this study, the authors reported an increase in cyclic electron transport in the BS cell of *Setaria viridis*, a C_4 NADP-ME plant, associated with the decrease in BS size in plants acclimated to low light conditions when compared to plants acclimated under high light. To bring the architecture of our maize model closer to one of *Setaria viridis*, PPDK and PEP-CK were blocked in the BS cell, leaving NADP-ME as the sole operational decarboxylation enzyme, while PSII was enabled in the BS cell. Additionally, M and BS photorespiratory Rubisco were also blocked to ensure C_4 photosynthesis was performed.

Based on the parameters provided in [61], two different scenarios were defined. In the high light (HL) uptake scenario, $AB_{\frac{BS}{M}}$ was set to 0.414, P_{Total} was set to 1000 μmol s^{-1} and $V_{\frac{BS}{M}}$ was set to 1.38. In the low light (LL) uptake scenario, $AB_{\frac{BS}{M}}$ was set to 0.343, P_{Total} was set at 350 μmol s^{-1} and $V_{\frac{BS}{M}}$ was set at 1.37. $AB_{\frac{BS}{M}}$ and P_{Total} values were taken directly from [61], while $V_{\frac{BS}{M}}$ was calculated based on provided IVD and V_{Width} values and equation 5. For each scenario, a budget plot of plastoquinone was obtained to evaluate linear and cyclic electron transport (Figure 20).

Analysis of the budget plot reveals that no NDH activity is detected in the HL scenario i.e that the BS cell is fully operating linear electron transport. In the LL scenario, 73% of plastoquinone flux is consumed by NDH thereby participating in cyclic electron transport. This increase in cyclic electron transport activity matches those reported by [61]. This reinforces our previous

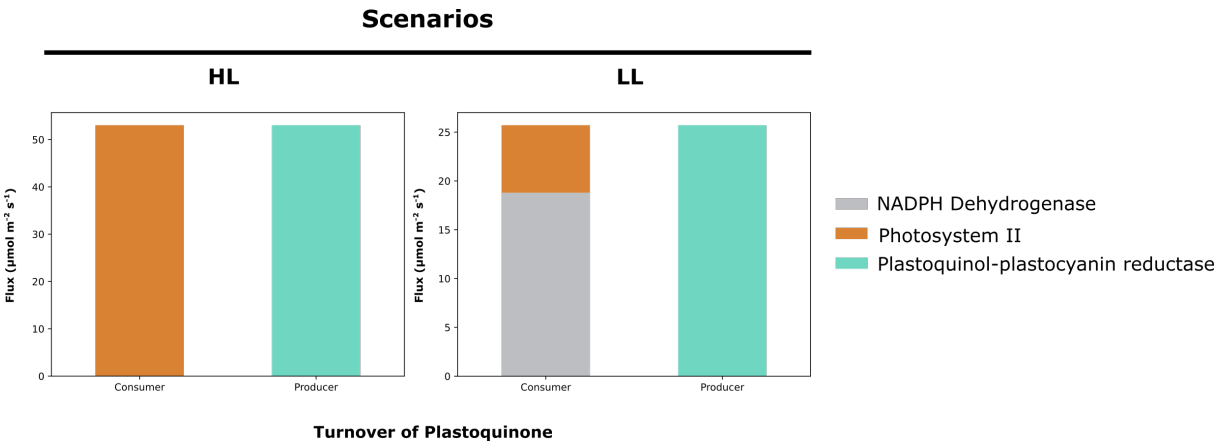

Figure 20 – Budget plots for plastoquinone turnover under high light (HL) and low light (LL) scenarios. In each plot, metabolite consuming fluxes are presented on the left side, while metabolite-producing fluxes are produced on the right.

observations of the connection between cyclic electron transport in the BS leading to higher ATP production in light-limiting conditions. Despite the lack of PEP-CK derived demand for ATP in this experiment, NADP-ME C_4 subtype can supply the BS cell with reducing power transferred from the M cell in the form of malate. The lack of NADPH production in the BS also removes demand for O_2 in the BS, reducing photorespiration and leaving room for the BS cell to specialize in ATP production to meet cellular demands.

In the dataset used for this experiment, P_{Total} values of the LL scenario were parameterized to 300 μmol s^{-1}. The value of 350 μmol s^{-1} was used instead for two reasons. Firstly, the implementation of $P_{Total} = 300\,\mu mol\,s^{-1}$ yielded no cyclic electron transport activity in the BS. This relates to the second reason, for this implementation did not yield the P_{BS} or P_M reported by [61], because in our implementation these values are calculated as a function of not only P_{Total} and $AB_{\frac{BS}{M}}$, but also of $V_{\frac{BS}{M}}$, which made the experimental conditions more difficult to replicate, and made it necessary to adjust the P_{Total} value to approximate so that the simulated P_{BS} value would match the one reported. These results also imply that the C_4 model possesses a minimum P_{Total} and P_{BS} value below which BS cell exclusive production of ATP is no longer feasible as an optimal solution under the presented constraints.

4.6 Impact of anatomical constraints on ATP Production

Leaf anatomy and ATP production are connected by the photosynthetic pathway. Leaf anatomy influences light penetration to the tissues, which therefore determines the cellular capacity for light-dependent ATP synthesis. It is then expected that the introduction of anatomical constraints in the model in the form of $V_{\frac{BS}{M}}$ would have an effect on M and BS cell comparative ATP production. In the following subchapter, we will show the results of an experiment designed to test this relationship. We have calculated, for selected flux distributions, the sum of all ATP producing fluxes normalized by their stoichiometry ($JATP$) for the M cell ($JATP_M$) and for the BS cell ($JATP_{BS}$). We then computed the ratio between them using equation 14.

$$JATP_{\frac{BS}{M}} = \frac{JATP_{BS} \cdot V_{BS}}{JATP_M \cdot V_M} \tag{14}$$

We proceeded to use this value to evaluate flux solutions against bibliographically established ($JATP_{\frac{BS}{M}}$) values.

4.6.1 Anatomical constraints improve JATP ratio prediction under a range of light uptake conditions in the C_4 model

To assess $JATP_{\frac{BS}{M}}$ value variation with changing light uptakes and anatomical constraints, flux solutions were obtained for a range of combinations of $AB_{\frac{BS}{M}}$ and P_{Total} values for two volume constrain scenarios. Before performing the simulations, M and BS photorespiratory Rubisco were blocked to ensure photosynthesis was performed through the C_4 cycle. In the first scenario, the cell types were assumed to have the same value i.e no anatomical constraint. In the second scenario, $V_{\frac{BS}{M}}$ was set at 5.3. This value was obtained from maize IVD and V_{Width} values derived from the datasets presented by [131]. For each of these flux solutions, $JATP_M$ and $JATP_{BS}$ were computed and $JATP_{\frac{BS}{M}}$ was obtained. From this data, 1 heatmap was generated for each scenario and a comparative analysis was formulated (Figure 21).

A similar distribution of $JATP_{\frac{BS}{M}}$ values is observed in both heatmaps, with higher $AB_{\frac{BS}{M}}$ values and lower P_{Total} values generating the higher $JATP_{\frac{BS}{M}}$, and vice-versa. Despite the

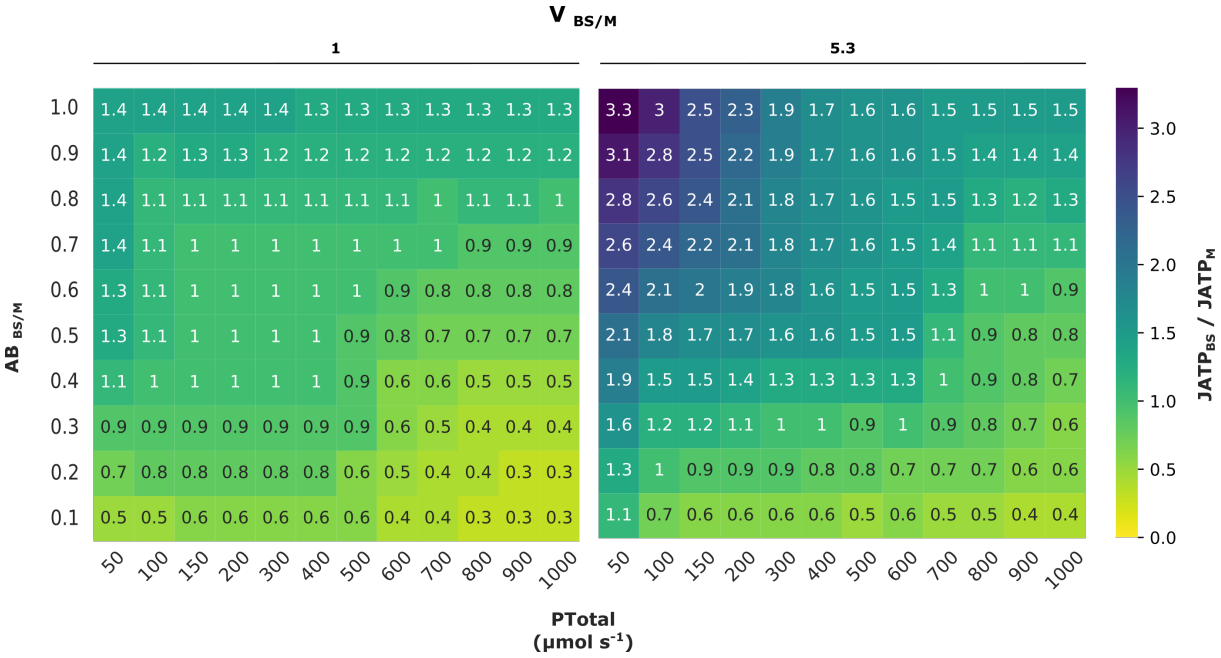

Figure 21 – Heatmaps representing the ratio between BS and M cell ATP production ($JATP_{\frac{BS}{M}}$) for two volume constraint scenarios. For each scenario, $JATP_{\frac{BS}{M}}$ was evaluated for a range of light uptakes and distributions. $JATP_{\frac{BS}{M}}$ values are represented rounded to the first decimal in each square and by colour through the colourmap.

similarities, in the scenario where the volume constrain is implemented, we observe a much wider range of $JATP_{\frac{BS}{M}}$ values, ranging from 0.4-3.3, while in the no volume constraint scenario ratios only vary between 1.4-0.3.

In the same paper where the anatomical measurements were derived, the authors reported a $JATP_{\frac{BS}{M}}$ value for maize of 1,37 under a $AB_{\frac{BS}{M}}$ of 0.66. Looking at the heatmaps, we identified $P_{Total} = 700$ μmol m^{-2} s^{-1} as the point were $JATP_{\frac{BS}{M}}$ value were closer to the ones reported when the volume constraint was implemented. We obtained the $JATP_{\frac{BS}{M}}$ for this point in both scenarios, and this information is displayed in Table 7.

Analysis of these results shows us that for this P_{Total} and $AB_{\frac{BS}{M}}$ scenario, the volume constrain improves $JATP_{\frac{BS}{M}}$ prediction compared to the bibliographically reported value. Looking back at the heatmaps yields that, in the absence of volume constraint implementation, $JATP_{\frac{BS}{M}}$ overall only come close to reported $JATP_{\frac{BS}{M}}$ values under biologically unrealistic parameters, such as extremely low light uptakes.

After analysing these two scenarios, we wanted to test how $JATP_{\frac{BS}{M}}$ values would behave under a range of different $V_{\frac{BS}{M}}$ values and light uptake conditions. To test this, a gradient of 6 $V_{\frac{BS}{M}}$

Table 7 – Table reporting the value of photon uptake (P_{Total}), light distribution between BS and M ($AB_{\frac{BS}{M}}$) and ratio of ATP production between BS and M ($JATP_{\frac{BS}{M}}$) for two flux solutions of the C_4 model and values reported in bibliographic sources. In the bibliography, no P_{Total} value was provided.

	$V_{\frac{BS}{M}}$		Bibliography
	1	**5.3**	**[131]**
$\mathbf{P_{Total}}$	700 μmol s^{-1}		n.a
$\boldsymbol{AB_{\frac{BS}{M}}}$	0.66		
$\boldsymbol{JATP_{\frac{BS}{M}}}$	0.93	1.37	1.32

where chosen and implemented for the same ranges of $AB_{\frac{BS}{M}}$ and P_{Total} previously used and $JATP_{\frac{BS}{M}}$ values were calculated. This resulted effectively in a parameter scan of $JATP_{\frac{BS}{M}}$ under different $V_{\frac{BS}{M}}$ conditions (Figure 22).

Observation of the parameter scans reveals a linear relationship between the increase in $V_{\frac{BS}{M}}$ and the range of values of $JATP_{\frac{BS}{M}}$. The same pattern is observed in all heatmaps, which was already described for $V_{\frac{BS}{M}} = 1$. The reported value of $JATP_{\frac{BS}{M}} = 1.32$ can be approximated in the $AB_{\frac{BS}{M}} = 0.66$ at when P_{Total} takes the value of 200 μmol s^{-1} under a $V_{\frac{BS}{M}}$ of 2. This optimum P_{Total} value increases when $V_{\frac{BS}{M}}$ takes the values of 3 and 4 to 400 and 600 μmol s^{-1}, respectively. When $V_{\frac{BS}{M}} = 5$, optimum $JATP_{\frac{BS}{M}}$ values are observed when $P_{Total} = 700\,\mu mol\,s^{-1}$). From these results, we can link $JATP_{\frac{BS}{M}}$ with plant anatomy (represented by $JATP_{\frac{BS}{M}} = 1.32$) and light uptake constraints (represented by P_{Total} and $AB_{\frac{BS}{M}}$). These parameters are different across the C_4 spectrum, and this model may allow us to make accurate predictions of energy metabolism for these species using these parameters as a starting point.

4.7 Biomass optimums under low light conditions predicted under low bundle sheath illumination

Besides investigating C, N and energy metabolism, we also investigated how the biomass value (pFBA objective function) would behave under varying $V_{\frac{BS}{M}}$ and $AB_{\frac{BS}{M}}$ under 3 P_{Total} scenarios: low (250 μmol s^{-1}) , medium (500 μmol s^{-1}) and high (750 μmol s^{-1}) light uptakes.

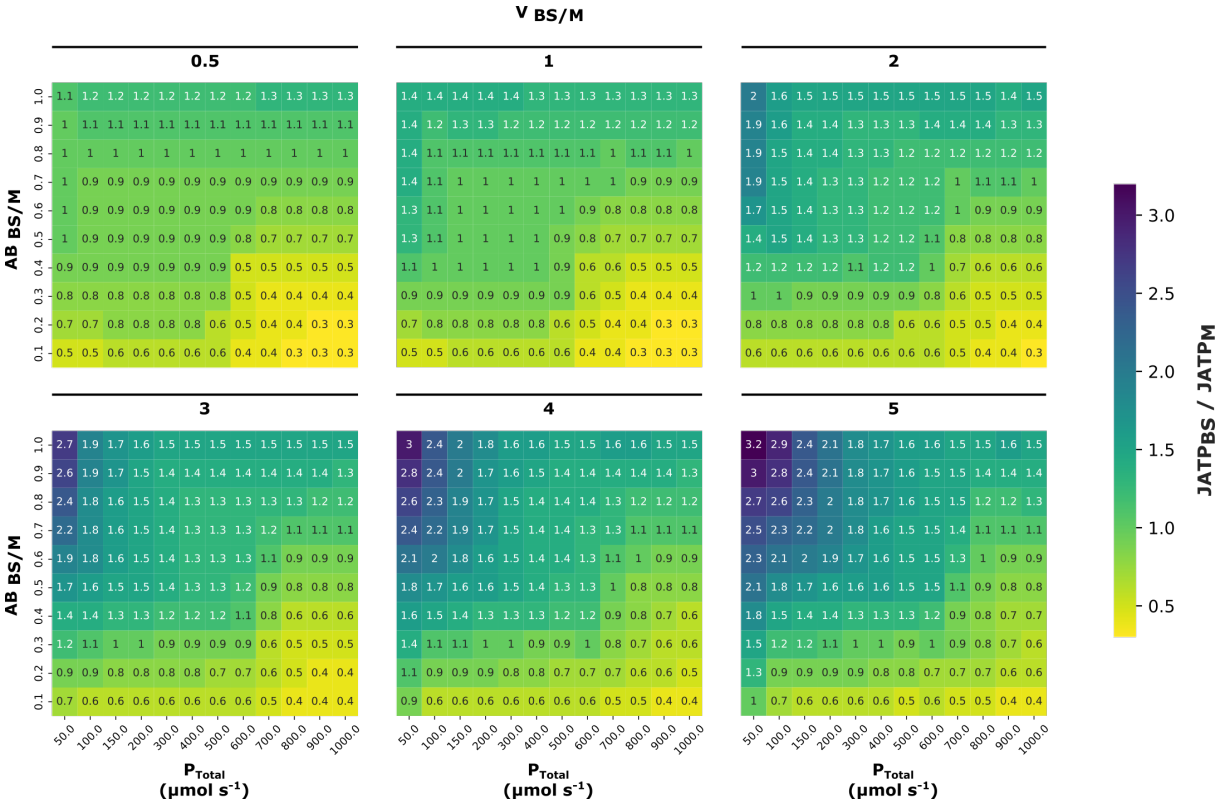

Figure 22 – Heatmaps representing the ratio between BS and M cell ATP production ($JATP_{\frac{BS}{M}}$) for six volume constraint scenarios. For each scenario, $JATP_{\frac{BS}{M}}$ was evaluated for a range of light uptakes and distributions. $JATP_{\frac{BS}{M}}$ values are represented rounded to the first decimal in each square and by colour through the colourmap.

For each of these scenarios, flux solutions were calculated for a range of $AB_{\frac{BS}{M}}$ and $V_{\frac{BS}{M}}$ values, and the biomass reaction flux value was computed. Additionally, M and BS photorespiratory Rubisco were blocked like in other simulations to ensure exclusive C_4 flux solutions. These values were then plotted to heatmaps (Figure 23).

Observation of the plots reveals that, under high light scenarios, biomass maintains a maximum value regardless of $AB_{\frac{BS}{M}}$ and $V_{\frac{BS}{M}}$ variation. This occurs because carbon uptake is limiting, and therefore the model cannot produce more biomass unless provided with more CO_2. When looking at the medium light uptake scenario, we observe that biomass assumes its lowest values under high $AB_{\frac{BS}{M}}$ and $V_{\frac{BS}{M}}$ values, which correspond to greater light uptake by the BS cell. The highest values for biomass are obtained when $AB_{\frac{BS}{M}} < 0.4$, mostly regardless of $V_{\frac{BS}{M}}$ value. When $AB_{\frac{BS}{M}} \geq 0.4$ it can be observed that the biomass optimum decreases with the increase in $V_{\frac{BS}{M}}$. A similar relationship between variables can be observed under low-light conditions. Under

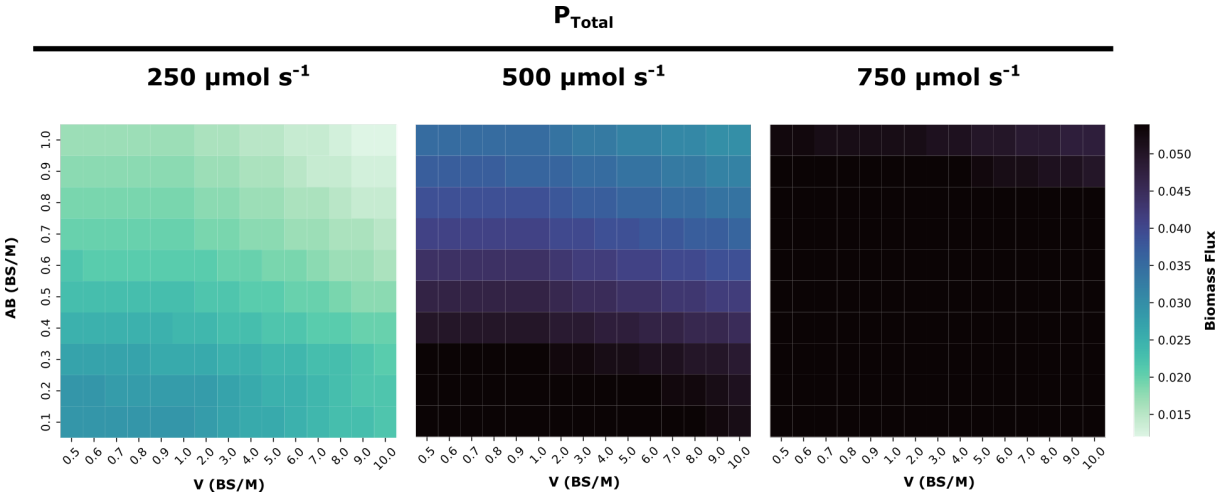

Figure 23 – Heatmaps representing the biomass flux value for 3 total photon uptake scenarios. For each scenario, the flux through the biomass reaction was evaluated for a range of light distributions and volume constraints. Biomass flux values are represented by colour through the colourmap.

these conditions, the highest biomass optimum flux values can be found under the lowest $AB_{\frac{BS}{M}}$ and $V_{\frac{BS}{M}}$ values, suggesting an inversely proportional relationship.

These results imply that, firstly, the increase or decrease in $V_{\frac{BS}{M}}$ does not affect the biomass optimum under light-saturated conditions; Secondly, that under light limiting conditions, higher $V_{\frac{BS}{M}}$ coupled with higher $AB_{\frac{BS}{M}}$ values yields suboptimal solutions with regards to biomass; Finally, the reduction of BS $V_{\frac{BS}{M}}$ coupled with lower $AB_{\frac{BS}{M}}$ values is associated with optimal biomass production under low light conditions. Coupled together these results suggest that characteristic high C_4 $V_{\frac{BS}{M}}$ and $AB_{\frac{BS}{M}}$ values are not sustainable under low light uptakes and are evolutionary characteristic acquired under conditions of light saturation.

4.8 General assumptions and limitations

In this subchapter we will review the major assumptions and limitations in our modelling approach approach.

Firstly, several experiments presented in this work are parameter scans for a given reaction flux or ratio under varying values of P_{Total}, $AB_{\frac{BS}{M}}$ and $V_{\frac{BS}{M}}$. The combination of these variables however can generate biologically irrealistic scenarios. Extremely low P_{Total} values (< 200 μmol s^{-1}) are unlikely unless under very shaded conditions. There is also a biological correlation

between $AB_{\frac{BS}{M}}$ and $V_{\frac{BS}{M}}$ values. Higher $V_{\frac{BS}{M}}$ values can lead to a lower "shading" effect by the M cells, due to the larger surface area of BS cells when compared to the M cells. This signifies that high $AB_{\frac{BS}{M}}$ values are unrealistic under low $V_{\frac{BS}{M}}$ and vice-versa. Additionally, it has been shown that increase in $AB_{\frac{BS}{M}}$ is a defining trait of C_4 evolution, who is accompanied by increased $V_{\frac{BS}{M}}$ values.

Secondly, to implement our modeling approach, we assumed that some areas of the leaf cross section are enriched in BS and others in M cells based on Kranz anatomy. In our framework, these areas are modeled separately as two different interacting systems. This was done in order to allow more flexible flux distributions of light uptake. In the related work of [17], one system was considered in which the two cell types existed in a theoretical area of 1 m^2 in which light uptake was allocated to each cell types through the application of $AB_{\frac{BS}{M}}$, which allocated a given light intensity to each cell type from an initial light intensity value. Our separate modeling approach considers different cellular volumes (translated into areas) for each cell type, requiring additional changes in the exchange between the cell types and subsequent normalization to enable flux comparison. Setting P_{Total} as an initial value to calculate P_M and P_{BS}, given values of $AB_{\frac{BS}{M}}$ and $V_{\frac{BS}{M}}$ allowed for an easier presentation of the results, but difficulted interpretation of the actual light intensities involved by not intuitively providing the actual values of P_M and P_{BS} for the flux solution.

Thirdly, chloroplast density and the actual light uptake capacity of the M and BS cells is modeled implicitly and is not parameterized in the model. Adding this information will be an asset for future modeling approaches.

Lastly, the usage of FBA to implement the model simulation also comes with its own set of drawbacks. First, FBA usage implies a constraints-based approach to modeling, in which enzymatic kinetic information is lacking; Second, the model does not consider the rate of metabolite diffusion between between the cell and the extracellular environment, or between the cytosol and the cellular compartments; Third, photorespiration rate is estimated based on its ratio with Rubisco carboxylase activity, but actual measured ratios are not available and therefore are not being implemented; Fourth, the effect of temperature is also not considered in the the model, and as such the effect of temperature on metabolic processes, such as photorespiration, is not modeled; Finally, cellular non-growth associated maintenance is applied through light-dependent maintenance, but the actual maintenance costs are neither known or implemented.

5

CONCLUSIONS

The main objective of this thesis contemplated the integration of anatomical constraints with a maize growing leaf model of C_4 photosynthesis with the goal of improving metabolic flux predictions. These constraints were then validated by evaluating flux predictions energy, carbon and nitrogen metabolism against bibliographic sources, with the additional description of biomass production.

Overviewing our main findings, we firstly observed that the model was capable of the individual and combined activity of NADP-ME and PEP-CK C_4 subtypes. Benchmarking against bibliographic sources revealed that the implementation of anatomical constraints improved flux predictions of C_2 photosynthesis and of the triose phosphate 3-phosphoglycerate shuttle, important pathways for the energy-balancing of C_4 flux mode.

Additionally, increased BS volume also improved the prediction of the cellular localization of NR and also helped identify the activity of GDH as a provider of NH_4^+ to be assimilated by the GS-GOGAT cycle. The deamination activity of GDH in maize BS had not been previously described in silico and provides comprehensive evidence for its biological role.

Furthermore, the choice of decarboxylation enzyme was affected by the variation of anatomical constraints, with PEP-CK activity being preferred when light is limiting, especially under low light uptakes by the BS (lower $AB_{\frac{BS}{M}}$ and $V_{\frac{BS}{M}}$ ratios). On the other side, NADP-ME is preferred under carbon limitation or higher light uptakes by the BS.

Moreover, generalization of the model for *Setaria viridis* anatomical and biochemical constraints allowed replication of the results of [61], predicting linear electron transport in the BS under high light conditions while cyclic electron transport was predicted under low light conditions.

Likewise, anatomical constraints improved predictions of $JATP_{\frac{BS}{M}}$ ratios when compared to the maize data of [131]. Broader analysis under a range of light conditions revealed a quasi-linear relationship between the anatomical constraints and $JATP_{\frac{BS}{M}}$ ratios, opening the possibility of generalization of this framework for other C_4 species given biochemical and anatomical measurements.

Finally, biomass production was not affected by anatomical constraints variation under carbon limiting conditions. However, under light limiting conditions, lower light uptakes by the BS lead to the optimal biomass solutions, coinciding with a preference for PEP-CK activity.

In summary, the implementation of anatomical constraints into the maize C_4 model improved flux predictions of C_4 metabolism. To the best of our knowledge, this is the first time such constraints are applied in a C_4 CBM framework. These constraints are important additions for the future inclusion of parameters such as enzyme kinetics, molecular crowding and cellular storage capacity. This work represents a step in obtaining plant metabolic models with increased accurate flux prediction capacity, which can be used downstream to enable and guide future metabolic engineering strategies.

5.1 Future perspectives

Future research direction with the C_4 model will involve strategies to improve the model's prediction accuracy and to improve the analysis of its outputs. This will be achieved by integrating the generic model with biochemical and anatomical constraints of other C_4 species and/or integrating with omics data to generate context-specific models. Additionally, model visualization and flux data analysis will be key in facilitating knowledge extraction from model predictions, either by application of graph-based visualization tools in small-scale analysis or by applying machine learning algorithms to interpret and compare large-scale model results. Lastly, the curation of the model is an ongoing process, which needs to be updated as new information becomes available or specific issues are detected, such as missing reactions or incorrect stoichiometries. Overall, these new directions will be able to generate models better capable of informing plant biologists and breeders about the inner workings of plant primary metabolism.

BIBLIOGRAPHY

[1] Bhattacharya, A. (2019). Global Climate Change and Its Impact on Agriculture. In *Changing climate and resource use efficiency in plants* (pp. 1–50). Academic Press.

[2] Mahato, A. (2014). Climate Change and its Impact on Agriculture. *International Journal of Scientific and Research Publications*, *4*(4).

[3] Raza, A., Razzaq, A., Mehmood, S., Zou, X., Zhang, X., Lv, Y., & Xu, J. (2019). Impact of Climate Change on Crops Adaptation and Strategies to Tackle Its Outcome: A Review. *Plants*, *8*(2), 34.

[4] Bruinsma, J. (2017). World agriculture: Towards 2015/2030: An FAO Study. *World Agriculture: Towards 2015/2030: An FAO Study*, 1–431.

[5] United Nations, Department of Economic and Social Affairs, & Population Division. (2019). *World Population Prospects 2019: Highlights* (tech. rep.).

[6] Alexandratos, N., & Bruinsma, J. (2012). World agriculture towards 2030/2050: the 2012 revision. *WORLD AGRICULTURE*.

[7] Wheeler, T., & Von Braun, J. (2013). Climate change impacts on global food security. *Science*, *341*(6145), 508–513.

[8] Singh, J., Pandey, P., James, D., Chandrasekhar, K., Achary, V. M. M., Kaul, T., Tripathy, B. C., & Reddy, M. K. (2014). Enhancing C3 photosynthesis: an outlook on feasible interventions for crop improvement. *Plant Biotechnology Journal*, *12*(9), 1217–1230.

[9] Simkin, A. J., López-Calcagno, P. E., & Raines, C. A. (2019). Feeding the world: improving photosynthetic efficiency for sustainable crop production. *Journal of Experimental Botany*, *70*(4), 1119–1140.

[10] Shevela, D., Björn, L. O., & Govindjee. (2019). *Photosynthesis: Solar energy for life*.

[11] Sage, R. F., & McKown, A. D. (2006). Is C4 photosynthesis less phenotypically plastic than C3 photosynthesis?*. *Journal of Experimental Botany*, *57*(2), 303–317.

[12] Éva, C., Oszvald, M., & Tamás, L. (2019). Current and possible approaches for improving photosynthetic efficiency. *Plant Science*, *280*, 433–440.

[13] Hussain, S., Ulhassan, Z., Brestic, M., Zivcak, M., Weijun Zhou, Allakhverdiev, S. I., Yang, X., Safdar, M. E., Yang, W., & Liu, W. (2021). Photosynthesis research under climate change. *Photosynthesis Research*, *150*(1-3), 5–19.

[14] Long, S. P., Marshall-Colon, A., & Zhu, X. G. (2015). Meeting the Global Food Demand of the Future by Engineering Crop Photosynthesis and Yield Potential. *Cell*, *161*(1), 56–66.

[15] O'Brien, E. J., Monk, J. M., & Palsson, B. O. (2015). Using genome-scale models to predict biological capabilities. *Cell*, *161*(5), 971–987.

[16] Töpfer, N. (2021). Environment-coupled models of leaf metabolism. *Biochemical Society Transactions*, *0*(August 2020), 1–11.

[17] Blätke, M. A., & Bräutigam, A. (2019). Evolution of C4 photosynthesis predicted by constraint-based modelling. *bioRxiv*, *2*, 1–24.

[18] Stirbet, A., Lazár, D., Guo, Y., & Govindjee, G. (2020). Photosynthesis: basics, history and modelling. *Annals of Botany*, *126*, 511–537.

[19] Ort, D. R., & Yocum, C. F. (1996). *Oxygenic photosynthesis: The light reactions* (Vol. 4). Springer Science & Business Media.

[20] Buchanan, B. B. (2016). The carbon (formerly dark) reactions of photosynthesis. *Photosynthesis Research*, *128*(2), 215–217.

[21] von Caemmerer, S., & Evans, J. R. (2010). Enhancing C3 Photosynthesis. *Plant Physiology*, *154*(2), 589–592.

[22] Raines, C. A. (2011). Increasing Photosynthetic Carbon Assimilation in C3 Plants to Improve Crop Yield: Current and Future Strategies. *Plant Physiology*, *155*(1), 36–42.

[23] Long, S. P., Ainsworth, E. A., Leakey, A. D., Nösbsrger, J., & Ort, D. R. (2006). Food for thought: Lower-than-expected crop yield stimulation with rising CO2 concentrations. *Science*, *312*(5782), 1918–1921.

[24] South, P. F., Cavanagh, A. P., Lopez-Calcagno, P. E., Raines, C. A., & Ort, D. R. (2018). Optimizing photorespiration for improved crop productivity. *Journal of Integrative Plant Biology*, *60*(12), 1217–1230.

[25] Peterhansel, C., Horst, I., Niessen, M., Blume, C., Kebeish, R., Kürkcüoglu, S., & Kreuzaler, F. (2010). Photorespiration. *https://doi.org/10.1199/tab.0130*, *2010*(8), e0130.

[26] Ehleringer, J. R., & Cerling, T. E. (2002). C3 and C4 photosynthesis. *Encyclopedia of global environmental change*, *2*(4).

[27] Muhaidat, R., Sage, T. L., Frohlich, M. W., Dengler, N. G., & Sage, R. F. (2011). Characterization of C3–C4 intermediate species in the genus Heliotropium L. (Boraginaceae): anatomy, ultrastructure and enzyme activity. *Plant, Cell & Environment*, *34*(10), 1723–1736.

[28] Sage, R. F., Khoshravesh, R., & Sage, T. L. (2014). From proto-Kranz to C4 Kranz: building the bridge to C4 photosynthesis. *Journal of experimental botany*, *65*(13), 3341–3356.

[29] Yoshimura, Y., Kubota, F., & Ueno, O. (2004). Structural and biochemical bases of photorespiration in C4 plants: Quantification of organelles and glycine decarboxylase. *Planta*, *220*(2), 307–317.

[30] Bellasio, C. (2017). A generalized stoichiometric model of C3, C2, C2+C4, and C4 photosynthetic metabolism. *Journal of Experimental Botany*, *68*(2), 269–282.

[31] Sage, R. F., Sage, T. L., & Kocacinar, F. (2012). Photorespiration and the Evolution of C_4 Photosynthesis. *Annual Review of Plant Biology*, *63*(1), 19–47.

[32] Wang, Y., Bräutigam, A., Weber, A. P., & Zhu, X. G. (2014). Three distinct biochemical subtypes of C4 photosynthesis? A modelling analysis. *Journal of Experimental Botany*, *65*(13), 3567–3578.

[33] Sage, R. F. (2004). The evolution of C4 photosynthesis. *New Phytologist*, *161*(2), 341–370.

[34] Bräutigam, A., & Gowik, U. (2016). Photorespiration connects C ¡sub¿3¡/sub¿ and C ¡sub¿4¡/sub¿ photosynthesis. *Journal of Experimental Botany*, *67*(10), 2953–2962.

[35] Töpfer, N., Braam, T., Shameer, S., Ratcliffe, R. G., & Sweetlove, L. J. (2020). Alternative Crassulacean Acid Metabolism Modes Provide Environment-Specific Water-Saving Benefits in a Leaf Metabolic Model. *The Plant Cell*, *32*(12), 3689–3705.

[36] Garcia, T. M., Heyduk, K., Kuzmick, E., & Mayer, J. A. (2014). Crassulacean acid metabolism biology. *New Phytologist*, *204*(4), 738–740.

[37] Gilman, I. S., & Edwards, E. J. (2020). Crassulacean acid metabolism. *Current Biology*, *30*(2), R57–R62.

[38] Keeley, J. E. (1998). CAM Photosynthesis in Submerged Aquatic Plants. *Botanical Review*, *64*(2), 121–175.

[39] Pribil, M., & Leister, D. (2016). Photosynthesis. *Encyclopedia of Applied Plant Sciences*, *1*, 90–95.

[40] Bonora, M., Patergnani, S., Rimessi, A., de Marchi, E., Suski, J. M., Bononi, A., Giorgi, C., Marchi, S., Missiroli, S., Poletti, F., Wieckowski, M. R., & Pinton, P. (2012). ATP synthesis and storage. *Purinergic Signalling*, *8*(3), 343–357.

[41] Nolfi-Donegan, D., Braganza, A., & Shiva, S. (2020). Mitochondrial electron transport chain: Oxidative phosphorylation, oxidant production, and methods of measurement. *Redox Biology*, *37*, 101674.

[42] Gardeström, P., & Igamberdiev, A. U. (2016). The origin of cytosolic ATP in photosynthetic cells. *Physiologia plantarum*, *157*(3), 367–379.

[43] Braun, H. P. (2020). The Oxidative Phosphorylation system of the mitochondria in plants. *Mitochondrion*, *53*, 66–75.

[44] Taiz, L., & Zeiger, E. (2010). *Plant Physiology* (5th ed.). Sinauer Associates Inc.

[45] Smith, E. N., Schwarzländer, M., Ratcliffe, R. G., & Kruger, N. J. (2021). Shining a light on NAD- and NADP-based metabolism in plants. *Trends in Plant Science*, *26*(10), 1072–1086.

[46] Hashida, S. N., & Kawai-Yamada, M. (2019). Inter-Organelle NAD Metabolism Underpinning Light Responsive NADP Dynamics in Plants. *Frontiers in Plant Science*, *10*, 960.

[47] Hashida, S. N., Takahashi, H., & Uchimiya, H. (2009). The role of NAD biosynthesis in plant development and stress responses. *Annals of Botany*, *103*(6), 819–824.

[48] Wang, C., Huang, X., Li, Q., Zhang, Y., Li, J. L., & Mou, Z. (2019). Extracellular pyridine nucleotides trigger plant systemic immunity through a lectin receptor kinase/BAK1 complex. *Nature Communications 2019 10:1*, *10*(1), 1–16.

[49] Foyer, C. H., & Noctor, G. (2009). Redox Regulation in Photosynthetic Organisms: Signaling, Acclimation, and Practical Implications. *Antioxidants & redox signaling*, *11*(4), 861–905.

[50] Hunt, L., Lerner, F., & Ziegler, M. (2004). NAD – new roles in signalling and gene regulation in plants. *New Phytologist*, *163*(1), 31–44.

[51] Pétriacq, P., de Bont, L., Tcherkez, G., & Gakière, B. (2013). NAD. *Plant Signaling & Behavior*, *8*(1), e22477
doi: 10.4161/psb.22477.

[52] Aghdam, M. S., Palma, J. M., & Corpas, F. J. (2020). NADPH as a quality footprinting in horticultural crops marketability. *Trends in Food Science & Technology*, *103*, 152–161.

[53] Bendall, D. S., & Manasse, R. S. (1995). Cyclic photophosphorylation and electron transport. *Biochimica et Biophysica Acta (BBA) - Bioenergetics*, *1229*(1), 23–38.

[54] Utschig, L. M., Soltau, S. R., Mulfort, K. L., Niklas, J., & Poluektov, O. G. (2018). Z-scheme solar water splitting via self-assembly of photosystem I-catalyst hybrids in thylakoid membranes. *Chemical Science*, *9*(45), 8504–8512.

[55] Kramer, D. M., & Evans, J. R. (2011). The Importance of Energy Balance in Improving Photosynthetic Productivity. *Plant Physiology*, *155*(1), 70–78.

[56] Endo, T., Ishida, S., Sato, N. I., & Fumihiko. (2008). Chloroplastic NAD(P)H Dehydrogenase Complex and Cyclic Electron Transport around Photosystem I. *Molecules and Cells*, *25*(2), 158–162.

[57] Ma, M., Liu, Y., Bai, C., & Yong, J. W. H. (2021). The Significance of Chloroplast NAD(P)H Dehydrogenase Complex and Its Dependent Cyclic Electron Transport in Photosynthesis. *Frontiers in Plant Science*, *12*, 643.

[58] Nakajima Munekage, Y. (2016). Light harvesting and chloroplast electron transport in NADP-malic enzyme type C4 plants. *Current Opinion in Plant Biology*, *31*, 9–15.

[59] Munekage, Y. N., Eymery, F., Rumeau, D., Cuiné, S., Oguri, M., Nakamura, N., Yokota, A., Genty, B., & Peltier, G. (2010). Elevated Expression of PGR5 and NDH-H in bundle sheath chloroplasts in C4 flaveria species. *Plant and Cell Physiology*, *51*(4), 664–668.

[60] Ermakova, M., Danila, F. R., Furbank, R. T., & Caemmerer, S. (2020). On the road to C 4 rice: advances and perspectives. *The Plant Journal*, *101*(4), 940–950.

[61] Bellasio, C., & Ermakova, M. (2022). Reduction of bundle sheath size boosts cyclic electron flow in C_4 *Setaria viridis* acclimated to low light. *The Plant Journal*, *111*(5), 1223–1237.

[62] Krapp, A. (2015). Plant nitrogen assimilation and its regulation: a complex puzzle with missing pieces. *Current opinion in plant biology*, *25*, 115–122.

[63] Bloom, A. J. (2015). The increasing importance of distinguishing among plant nitrogen sources. *Current Opinion in Plant Biology*, *25*, 10–16.

[64] Andrews, M. (1986). The partitioning of nitrate assimilation between root and shoot of higher plants. *Plant, Cell and Environment*, *9*(7), 511–519.

[65] Xu, G., Fan, X., & Miller, A. J. (2012). Plant Nitrogen Assimilation and Use Efficiency. *http://dx.doi.org/10.1146/annurev-arplant-042811-105532*, *63*, 153–182.

[66] Meyer, C., & Stitt, M. (2001). Nitrate Reduction and signalling. *Plant Nitrogen*, 37–59.

[67] Kojima, S., Konishi, N., Beier, M. P., Ishiyama, K., Maru, I., Hayakawa, T., & Yamaya, T. (2014). NADH-dependent glutamate synthase participated in ammonium assimilation in Arabidopsis root. *https://doi.org/10.4161/psb.29402*, *9*(8).

[68] Heldt, H.-W., & Heldt, F. (2005). 10 - Nitrate assimilation is essential for the synthesis of organic matter. In H.-W. Heldt & F. B. T. .-. P. B. (E. Heldt (Eds.). Academic Press.

[69] Ghannoum, O., Evans, J. R., & von Caemmerer, S. (2011). Chapter 8 Nitrogen and Water Use Efficiency of C4 Plants BT - C4 Photosynthesis and Related CO2 Concentrating Mechanisms. In A. S. Raghavendra & R. F. Sage (Eds.). Springer Netherlands.

[70] Kopriva, S., & Koprivova, A. (2005). Sulfate assimilation and glutathione synthesis in C4 plants. *Photosynthesis Research*, *86*(3), 363–372.

[71] Weckopp, S. C., & Kopriva, S. (2015). Are changes in sulfate assimilation pathway needed for evolution of C4 photosynthesis? *Frontiers in Plant Science*, *5*(JAN), 773.

[72] Jobe, T. O., Zenzen, I., Rahimzadeh Karvansara, P., & Kopriva, S. (2019). Integration of sulfate assimilation with carbon and nitrogen metabolism in transition from C3 to C4 photosynthesis. *Journal of Experimental Botany*, *70*(16), 4211–4221.

[73] Kopriva, S. (2011). Chapter 7 Nitrogen and Sulfur Metabolism in C4 Plants. In A. S. Raghavendra & R. F. Sage (Eds.), *C4 photosynthesis and related co2 concentrating mechanisms* (pp. 109–128). Springer Netherlands.

[74] Raman, K., & Chandra, N. (2009). Flux balance analysis of biological systems: applications and challenges. *Briefings in Bioinformatics*, *10*(4), 435–449.

[75] Anand, S., Mukherjee, K., & Padmanabhan, P. (2020). An insight to flux-balance analysis for biochemical networks. *https://doi.org/10.1080/02648725.2020.1847440*, *36*(1), 32–55.

[76] Bordbar, A., Feist, A. M., Usaite-Black, R., Woodcock, J., Palsson, B. O., & Famili, I. (2011). A multi-tissue type genome-scale metabolic network for analysis of whole-body systems physiology. *BMC Systems Biology*, *5*(1), 1–17.

[77] Orth, J. D., Thiele, I., & Palsson, B. O. (2010). What is flux balance analysis? *Nature Biotechnology*, *28*(3), 245–248.

[78] Lewis, N. E., Hixson, K. K., Conrad, T. M., Lerman, J. A., Charusanti, P., Polpitiya, A. D., Adkins, J. N., Schramm, G., Purvine, S. O., Lopez-Ferrer, D., Weitz, K. K., Eils, R., König, R., Smith, R. D., & Palsson, B. Ø. (2010). Omic data from evolved E. coli are consistent

with computed optimal growth from genome-scale models. *Molecular Systems Biology*, *6*(1), 390.

[79] Holzhütter, H. G. (2004). The principle of flux minimization and its application to estimate stationary fluxes in metabolic networks. *European Journal of Biochemistry*, *271*(14), 2905–2922.

[80] Jenior, M. L., Moutinho, T. J., Dougherty, B. V., & Papin, J. A. (2020). Transcriptome-guided parsimonious flux analysis improves predictions with metabolic networks in complex environments. *PLOS Computational Biology*, *16*(4), e1007099.

[81] Mahadevan, R., & Schilling, C. H. (2003). The effects of alternate optimal solutions in constraint-based genome-scale metabolic models. *Metabolic Engineering*, *5*, 264–276.

[82] Gudmundsson, S., & Thiele, I. (2010). Computationally efficient flux variability analysis. *BMC Bioinformatics*, *11*(1), 1–3.

[83] Michael, T. P., & VanBuren, R. (2015). Progress, challenges and the future of crop genomes. *Current Opinion in Plant Biology*, *24*, 71–81.

[84] Kanehisa, M., Goto, S., Sato, Y., Kawashima, M., Furumichi, M., & Tanabe, M. (2014). Data, information, knowledge and principle: back to metabolism in KEGG. *Nucleic Acids Research*, *42*(D1), D199–D205.

[85] Seaver, S. M., Gerdes, S., Frelin, O., Lerma-Ortiz, C., Bradbury, L. M., Zallot, R., Hasnain, G., Niehaus, T. D., El Yacoubi, B., Pasternak, S., Olson, R., Pusch, G., Overbeek, R., Stevens, R., De Crécy-Lagard, V., Ware, D., Hanson, A. D., & Henry, C. S. (2014). High-throughput comparison, functional annotation, and metabolic modeling of plant genomes using the PlantSEED resource. *Proceedings of the National Academy of Sciences of the United States of America*, *111*(26), 9645–9650.

[86] Schläpfer, P., Zhang, P., Wang, C., Kim, T., Banf, M., Chae, L., Dreher, K., Chavali, A. K., Nilo-Poyanco, R., Bernard, T., Kahn, D., & Rhee, S. Y. (2017). Genome-Wide Prediction of Metabolic Enzymes, Pathways, and Gene Clusters in Plants. *Plant Physiology*, *173*(4), 2041–2059.

[87] Sweetlove, L. J., Nielsen, J., & Fernie, A. R. (2016). Engineering central metabolism - a grand challenge for plant biologists. *The Plant Journal*, *90*(4), 749–763.

[88] Williams, T. C., Poolman, M. G., Howden, A. J., Schwarzlander, M., Fell, D. A., Ratcliffe, R. G., & Sweetlove, L. J. (2010). A Genome-Scale Metabolic Model Accurately Predicts Fluxes in Central Carbon Metabolism under Stress Conditions. *Plant Physiology*, *154*(1), 311–323.

[89] Wang, C., Guo, L., Li, Y., & Wang, Z. (2012). Systematic Comparison of C3 and C4 Plants Based on Metabolic Network Analysis. *BMC Systems Biology*, *6*(SUPPL.2), 1–14.

[90] Rolletschek, H., Grafahrend-Belau, E., Munz, E., Radchuk, V., Kartäusch, R., Tschiersch, H., Melkus, G., Schreiber, F., Jakob, P. M., & Borisjuk, L. (2015). Metabolic Architecture of the Cereal Grain and Its Relevance to Maximize Carbon Use Efficiency. *Plant Physiology*, *169*(3), 1698–1713.

[91] Shaw, R., & Cheung, C. Y. (2018). A dynamic multi-tissue flux balance model captures carbon and nitrogen metabolism and optimal resource partitioning during arabidopsis growth. *Frontiers in Plant Science*, *9*, 884.

[92] Pfau, T., Christian, N., Masakapalli, S. K., Sweetlove, L. J., Poolman, M. G., & Ebenhöh, O. (2018). The intertwined metabolism during symbiotic nitrogen fixation elucidated by metabolic modelling. *Scientific Reports 2018 8:1*, *8*(1), 1–11.

[93] Hawkins, C., Ginzburg, D., Zhao, K., Dwyer, W., Xue, B., Xu, A., Rice, S., Cole, B., Paley, S., Karp, P., & Rhee, S. Y. (2021). Plant Metabolic Network 15: A resource of genome-wide metabolism databases for 126 plants and algae. *Journal of Integrative Plant Biology*, *63*(11), 1888–1905.

[94] de Oliveira Dal'Molin, C. G., Quek, L. E., Saa, P. A., & Nielsen, L. K. (2015). A multi-tissue genome-scale metabolic modeling framework for the analysis of whole plant systems. *Frontiers in Plant Science*, *6*(JAN), 1–12.

[95] Ryu, J. Y., Kim, H. U., & Lee, S. Y. (2015). Reconstruction of genome-scale human metabolic models using omics data. *Integrative Biology*, *7*(8), 859–868.

[96] Clark, T. J., Guo, L., Morgan, J., & Schwender, J. (2020). Modeling Plant Metabolism: From Network Reconstruction to Mechanistic Models. *Annual Review of Plant Biology*, *71*(1), 303–326.

[97] Poolman, M. G., Kundu, S., Shaw, R., & Fell, D. A. (2013). Responses to Light Intensity in a Genome-Scale Model of Rice Metabolism. *Plant Physiology*, *162*(2), 1060–1072.

[98] Chatterjee, A., Huma, B., Shaw, R., & Kundu, S. (2017). Reconstruction of Oryza sativa indica genome scale metabolic model and its responses to varying RuBisCO activity, light intensity, and enzymatic cost conditions. *Frontiers in Plant Science*, *8*, 2060.

[99] Arnold, A., & Nikoloski, Z. (2014). Bottom-up metabolic reconstruction of arabidopsis and its application to determining the metabolic costs of enzyme production. *Plant Physiology*, *165*(3), 1380–1391.

[100] Maurice Cheung, C. Y., Poolman, M. G., Fell, D. A., George Ratcliffe, R., & Sweetlove, L. J. (2014). A diel flux balance model captures interactions between light and dark metabolism during day-night cycles in C3 and crassulacean acid metabolism leaves. *Plant Physiology*, *165*(2), 917–929.

[101] Simons, M., Saha, R., Amiour, N., Kumar, A., Guillard, L., Clément, G., Miquel, M., Li, Z., Mouille, G., Lea, P. J., Hirel, B., & Maranas, C. D. (2014). Assessing the metabolic impact of nitrogen availability using a compartmentalized maize leaf genome-scale model. *Plant Physiology*, *166*(3), 1659–1674.

[102] Seaver, S. M., Bradbury, L. M., Frelin, O., Zarecki, R., Ruppin, E., Hanson, A. D., & Henry, C. S. (2015). Improved evidence-based genome-scale metabolic models for maize leaf, embryo, and endosperm. *Frontiers in Plant Science*, *6*(MAR), 142.

[103] Bogart, E., & Myers, C. R. (2016). Multiscale metabolic modeling of C4 plants: Connecting nonlinear genome-scale models to leaf-scale metabolism in developing maize leaves. *PLoS ONE*, *11*(3), e0151722.

[104] Yuan, H., Cheung, C. Y. M., Hilbers, P. A. J., & van Riel, N. A. W. (2016). Flux Balance Analysis of Plant Metabolism: The Effect of Biomass Composition and Model Structure on Model Predictions. *Frontiers in Plant Science*, *7*(APR2016), 537.

[105] Botero, K., Restrepo, S., & Pinzón, A. (2018). A genome-scale metabolic model of potato late blight suggests a photosynthesis suppression mechanism 06 Biological Sciences 0607 Plant Biology. *BMC Genomics*, *19*(S8), 863.

[106] Mallmann, J., Heckmann, D., Bräutigam, A., Lercher, M. J., Weber, A. P., Westhoff, P., & Gowik, U. (2014). The role of photorespiration during the evolution of C4 photosynthesis in the genus Flaveria. *eLife*, *2014*(3).

[107] Shameer, S., Baghalian, K., Cheung, C. Y. M., Ratcliffe, R. G., & Sweetlove, L. J. (2018). Computational analysis of the productivity potential of CAM. *Nature Plants*, *4*(3), 165–171.

[108] Nikoloski, Z., Perez-Storey, R., & Sweetlove, L. J. (2015). Inference and prediction of metabolic network fluxes. *Plant Physiology*, *169*(3), 1443–1455.

[109] Sweetlove, L. J., & George Ratcliffe, R. (2011). Flux-balance modeling of plant metabolism. *Frontiers in Plant Science*, *2*(AUG), 1–10.

[110] Chandrasekaran, S., & Price, N. D. (2010). Probabilistic integrative modeling of genome-scale metabolic and regulatory networks in Escherichia coli and Mycobacterium tuberculosis. *Proceedings of the National Academy of Sciences of the United States of America*, *107*(41), 17845–17850.

[111] Shlomi, T., Cabili, M. N., Herrgård, M. J., Palsson, B., & Ruppin, E. (2008). Network-based prediction of human tissue-specific metabolism. *Nature Biotechnology 2008 26:9*, *26*(9), 1003–1010.

[112] Jensen, P. A., & Papin, J. A. (2011). Functional integration of a metabolic network model and expression data without arbitrary thresholding. *Bioinformatics*, *27*(4), 541–547.

[113] Becker, S. A., & Palsson, B. O. (2008). Context-Specific Metabolic Networks Are Consistent with Experiments. *PLOS Computational Biology*, *4*(5), e1000082.

[114] Töpfer, N., Jozefczuk, S., & Nikoloski, Z. (2012). Integration of time-resolved transcriptomics data with flux-based methods reveals stress-induced metabolic adaptation in Escherichia coli. *BMC Systems Biology*, *6*(1), 1–10.

[115] Colijn, C., Brandes, A., Zucker, J., Lun, D. S., Weiner, B., Farhat, M. R., Cheng, T. Y., Moody, D. B., Murray, M., & Galagan, J. E. (2009). Interpreting Expression Data with Metabolic Flux Models: Predicting Mycobacterium tuberculosis Mycolic Acid Production. *PLOS Computational Biology*, *5*(8), e1000489.

[116] De Oliveira Dal'Molin, C. G., Orellana, C., Gebbie, L., Steen, J., Hodson, M. P., Chrysanthopoulos, P., Plan, M. R., McQualter, R., Palfreyman, R. W., & Nielsen, L. K. (2016).

Metabolic reconstruction of setaria italica: A systems biology approach for integrating tissue-specific omics and pathway analysis of bioenergy grasses. *Frontiers in Plant Science*, *7*(AUG2016), 1138.

[117] Poolman, M. G., Miguet, L., Sweetlove, L. J., & Fell, D. A. (2009). A genome-scale metabolic model of Arabidopsis and some of its properties. *Plant Physiology*, *151*(3), 1570–1581.

[118] Edwards, G. E., Furbank, R. T., Hatch, M. D., & Osmond, C. B. (2001). What Does It Take to Be C4? Lessons from the Evolution of C4 Photosynthesis. *Plant Physiology*, *125*(1), 46–49.

[119] Lundgren, M. R., Osborne, C. P., & Christin, P. A. (2014). Deconstructing Kranz anatomy to understand C4 evolution. *Journal of Experimental Botany*, *65*(13), 3357–3369.

[120] Hattersley, P. W., Watson, L., & Osmond, C. B. (1977). In situ Immunofluorescent Labelling of Ribulose-1,5-Bisphosphate Carboxylase in Leaves of C3 and C4 Plants. *Functional Plant Biology*, *4*(4), 523–539.

[121] Leegood, R. C. (2002). C4 photosynthesis: principles of CO2 concentration and prospects for its introduction into C3 plants. *Journal of Experimental Botany*, *53*(369), 581–590.

[122] Von Caemmerer, S., & Furbank, R. T. (2003). The C4 pathway: an efficient CO2 pump. *Photosynthesis Research 2003 77:2*, *77*(2), 191–207.

[123] Edwards, G. E., & Voznesenskaya, E. V. (2011). Chapter 4 C4 Photosynthesis: Kranz Forms and Single-Cell C4 in Terrestrial Plants BT - C4 Photosynthesis and Related CO2 Concentrating Mechanisms. In A. S. Raghavendra & R. F. Sage (Eds.). Springer Netherlands.

[124] Nelson, T. (2011). Chapter 9 Development of Leaves in C4 Plants: Anatomical Features That Support C4 Metabolism BT - C4 Photosynthesis and Related CO2 Concentrating Mechanisms. In A. S. Raghavendra & R. F. Sage (Eds.). Springer Netherlands.

[125] Gowik, U., & Westhoff, P. (2011). The Path from C3 to C4 Photosynthesis. *Plant Physiology*, *155*(1), 56–63.

[126] Bissinger, K., Khoshrvesh, R., Kotrade, J. P., Oakley, J., Sage, T. L., Sage, R. F., Hartmann, H. E., & Kadereit, G. (2014). Gisekia (Gisekiaceae): Phylogenetic relationships, biogeography, and ecophysiology of a poorly known C4 lineage in the Caryophyllales. *American Journal of Botany*, *101*(3), 499–509.

[127] Mertz, R. A., & Brutnell, T. P. (2014). Bundle sheath suberization in grass leaves: multiple barriers to characterization. *Journal of Experimental Botany*, *65*(13), 3371–3380.

[128] Aliyeva, N. K., Aliyeva, D. R., Suleymanov, S. Y., Rzayev, F. H., Gasimov, E. K., & Huseynova, I. M. (2020). Biochemical properties and ultrastructure of mesophyll and bundle sheath thylakoids from maize (Zea mays) chloroplasts. *Functional plant biology : FPB*, *47*(11), 970–976.

[129] Romanowska, E., Kargul, J., Powikrowska, M., Finazzi, G., Nield, J., Drozak, A., & Pokorska, B. (2008). Structural organization of photosynthetic apparatus in agranal chloroplasts of maize. *The Journal of biological chemistry*, *283*(38), 26037–26046.

[130] Christin, P. A., Osborne, C. P., Chatelet, D. S., Columbus, J. T., Besnard, G., Hodkinson, T. R., Garrison, L. M., Vorontsova, M. S., & Edwards, E. J. (2013). Anatomical enablers and the evolution of C4 photosynthesis in grasses. *Proceedings of the National Academy of Sciences of the United States of America*, *110*(4), 1381–1386.

[131] Bellasio, C., & Lundgren, M. R. (2016). Anatomical constraints to C4 evolution: light harvesting capacity in the bundle sheath. *New Phytologist*, *212*(2), 485–496.

[132] Ebrahim, A., Lerman, J. A., Palsson, B. O., & Hyduke, D. R. (2013). COBRApy: COnstraints-Based Reconstruction and Analysis for Python. *BMC Systems Biology*, *7*(1), 1–6.

[133] Häusler, R. E., Hirsch, H.-J., Kreuzaler, F., & Peterhänsel, C. (2002). Overexpression of C4-cycle enzymes in transgenic C3 plants: a biotechnological approach to improve C3-photosynthesis. *Journal of Experimental Botany*, *53*(369), 591–607.

[134] Shameer, S., Ratcliffe, R. G., & Sweetlove, L. J. (2019). Leaf Energy Balance Requires Mitochondrial Respiration and Export of Chloroplast NADPH in the Light. *Plant Physiology*, *180*(4), 1947–1961.

[135] Saha, R., Suthers, P. F., & Maranas, C. D. (2011). Zea mays irs1563: A comprehensive genome-scale metabolic reconstruction of maize metabolism. *PLoS ONE*, *6*(7).

[136] Caspi, R., Altman, T., Billington, R., Dreher, K., Foerster, H., Fulcher, C. A., Holland, T. A., Keseler, I. M., Kothari, A., Kubo, A., Krummenacker, M., Latendresse, M., Mueller, L. A., Ong, Q., Paley, S., Subhraveti, P., Weaver, D. S., Weerasinghe, D., Zhang, P., & Karp, P. D. (2014). The MetaCyc database of metabolic pathways and enzymes and the BioCyc collection of Pathway/Genome Databases. *Nucleic Acids Research*, *42*(D1), D459–D471.

[137] Linka, N., & Weber, A. P. (2010). Intracellular Metabolite Transporters in Plants. *Molecular Plant*, *3*(1), 21–53.

[138] Yin, X., Van Der Putten, P. E., Driever, S. M., & Struik, P. C. (2016). Temperature response of bundle-sheath conductance in maize leaves. *Journal of Experimental Botany*, *67*(9), 2699–2714.

[139] Leakey, A. D., Uribelarreà, M., Ainsworth, E. A., Naidu, S. L., Rogers, A., Ort, D. R., & Long, S. P. (2006). Photosynthesis, Productivity, and Yield of Maize Are Not Affected by Open-Air Elevation of CO2 Concentration in the Absence of Drought. *Plant Physiology*, *140*(2), 779–790.

[140] Bellasio, C., & Griffiths, H. (2014). Acclimation of C4 metabolism to low light in mature maize leaves could limit energetic losses during progressive shading in a crop canopy. *Journal of Experimental Botany*, *65*(13), 3725–3736.

[141] Josse, E. M., Simkin, A. J., Gaffe, J., Laboure, A. M., Kuntz, M., & Carol, P. (2000). A plastid terminal oxidase associated with carotenoid desaturation during chromoplast differentiation. *Plant physiology*, *123*(4), 1427–1436.

[142] Reiser, J., Linka, N., Lemke, L., Jeblick, W., & Neuhaus, H. E. (2004). Molecular Physiological Analysis of the Two Plastidic ATP/ADP Transporters from Arabidopsis. *Plant Physiology*, *136*(3), 3524–3536.

[143] Ivanov, B., Asada, K., Kramer, D. M., & Edwards, G. (2005). Characterization of photosynthetic electron transport in bundle sheath cells of maize. I. Ascorbate effectively stimulates cyclic electron flow around PSI. *Planta*, *220*(4), 572–581.

[144] Twachtmann, M., Altmann, B., Muraki, N., Voss, I., Okutani, S., Kurisu, G., Hase, T., & Hanke, G. T. (2012). N-Terminal Structure of Maize Ferredoxin:NADP+ Reductase Determines Recruitment into Different Thylakoid Membrane Complexes. *The Plant Cell*, *24*(7), 2979–2991.

[145] Cheung, C. Y. M., Williams, T. C. R., Poolman, M. G., Fell, D. A., Ratcliffe, R. G., & Sweetlove, L. J. (2013). A method for accounting for maintenance costs in flux balance analysis improves the prediction of plant cell metabolic phenotypes under stress conditions. *The Plant Journal*, *75*(6), 1050–1061.

[146] Inkscape Project. (2020, April 16). *Inkscape* (Version 0.92.5).

[147] Zheng, Y., Xu, M., Shen, R., & Qiu, S. (2013). Effects of artificial warming on the structural, physiological, and biochemical changes of maize (Zea mays L.) leaves in northern China. *Acta Physiologiae Plantarum*, *35*(10), 2891–2904.

[148] Dubois, F., Tercé-Laforgue, T., Gonzalez-Moro, M.-B., Estavillo, J.-M., Sangwan, R., Gallais, A., & Hirel, B. (2003). Glutamate dehydrogenase in plants: is there a new story for an old enzyme? *Plant Physiology and Biochemistry*, *41*(6-7), 565–576.